Advanced Sensor and Energy Materials 2 (2023) 100061

Contents lists available at ScienceDirect

Advanced Sensor and Energy Materials

journal homepage: www.sciencedirect.com/journal/advanced-sensor-and-energy-materials

Review

Advances in ORR, OER, and HER of fullerenes and derivatives: From DFT calculations to experimental identification

Ao Yu [a], Nimanyu Joshi [a,b], Wei Zhang [a,b], Yang Yang [a,b,c,d,e,*]

[a] NanoScience Technology Center, University of Central Florida, Orlando, FL 32826, USA
[b] Department of Materials Science and Engineering, University of Central Florida, Orlando, FL 32826, USA
[c] Renewable Energy and Chemical Transformation Cluster, University of Central Florida, Orlando, FL 32826, USA
[d] Department of Chemistry, University of Central Florida, Orlando, FL 32826, USA
[e] The Stephen W. Hawking Center for Microgravity Research and Education, University of Central Florida, Orlando, FL 32826, USA

ARTICLE INFO

Keywords:
Fullerenes
Electrocatalysts
DFT calculations
Oxygen reduction reactions
Oxygen evolution reactions
Hydrogen evolution reactions

ABSTRACT

Fullerenes are widely applied in the field of ORR, OER, and HER due to their well-defined molecular structures, excellent electron affinity potential that can be used to regulate the electronic structures when composited with other materials, the π-π intermolecular self-assembly into super crystals, and the customizable chemical modifications including heteroatom doping, metal encapsulation, and functionalization. These advantages endow fullerene with a great number of derivates and composites. Many theoretical and experimental works are reported on electrocatalysts. To better understand the study progress, herein, we give a common review of the latest research. We first introduce the theoretical calculations of fullerenes and their derivates towards ORR, OER, and HER, aiming to give understandable reaction mechanisms and electrocatalytic active sites. Then, the experimental identification of the electrocatalytic performance was summarized. The experimental section is organized based on fullerene-based composites including fullerene/carbon composites, fullerene/sulfide composites, fullerene/LDH or metal composites, and fullerene molecular and its derivates including fullerene crystals, fullertubes, as well as endohedral fullerene. Finally, the challenges and opportunities for rational designing of electrocatalysts using fullerene as a precursor or additive are summarized and highlighted. The review not only points out the recent progress in fullerene application in electrocatalysts but also gives an in-depth insight into the materials design theoretically and experimentally that helps the future study directions.

1. Introduction

Fullerenes, constituted of sp^2-hybridized carbon atoms, are one of the allotropes of carbon that have drawn great attention for electrocatalytic applications in oxygen reduction reaction (ORR), oxygen evolution reaction (OER), and hydrogen evolution reaction (HER) [1–4]. They possess favorable electronic properties and π-conjugated curved surfaces with promoted catalytic performance, which can be attributed to the quantum restriction on the electronic states and the intrinsic pentagon carbon defects [5,6]. However, quantum confinement and intrinsic pentagon defects are highly concealed by their bulk counterparts, thus hindering exposure of the electrocatalytic active sites [5]. Moreover, when used in the aqueous electrocatalytic reaction including ORR, OER, and HER, the wide applications of fullerenes are greatly limited by their poor wettability and the low electronic conductivity that impede the charge transfer during the electrochemical process [7]. Nevertheless, continuous in-depth research shows exciting findings about the application of fullerenes via handling the pure fullerenes in theory and experiment. The theoretical density functional theory (DFT) studies have demonstrated that the heteroatom-doped and metal-encapsulated fullerenes have accurate chemical formulas and specific electronic structures, which also can be effective candidates to forecast the potential electrocatalytic performance [8–10]. In order to realize the theoretical activity and take full advantage of the beneficial characteristic of electrocatalytic performance, many particular works were reported. For example, the quantum confinement of fullerene was widely used to regular the base materials (like carbon nanotubes, metal oxides, and sulfides), thus forming composites with enhanced electrocatalytic

* Corresponding author.
E-mail address: Yang.Yang@ucf.edu (Y. Yang).

https://doi.org/10.1016/j.asems.2023.100061
Received 1 April 2023; Received in revised form 28 April 2023; Accepted 30 April 2023
Available online 3 May 2023

performance [1,11–13]. Besides, fullerenes can also be directly used to refine the metals, and then further construct uniform metal nanoparticle (NP) and single atom (SA) electrocatalysts with high efficiency [14]. Assembling fullerenes into crystals or co-crystals with specific micro-/nano-morphology by the liquid-liquid interfacial precipitation (LLIP) is an effective strategy to obtain homogeneous and heterogeneous catalysts, which can greatly enhance the catalytic performance [15]. Furthermore, functionalized fullerene with sufficient active groups greatly extends the fullerene-based derivatives, which not only can improve its conductivity and wettability, but also introduce active heteroatoms [16].

Fullerene-based electrocatalysts are currently being rapidly developed for various electrocatalytic applications. Making a detailed and systematic taxonomy of reported electrocatalysts is essential to understanding the progress of this fascinating research direction from theory to experiment. In this review, we first focus on the electrocatalytic mechanisms of fullerenes and their derivatives based on the DFT calculations. Guided by the DFT calculations, many experimental studies have been summarized. The applications of fullerene-based electrocatalysts can be classified into the following sections: ORR, OER, and HER.

2. DFT calculations

The increasing number of carbon atoms in fullerene molecules results in a larger number of isomers, which implies the existence of abundant hybridized molecular orbitals in fullerene molecules. For example, it has been shown theoretically that C_{60}, constructed with 60 sp^2-hybridized carbon atoms, has the highest occupied molecular orbitals (HOMO) and lowest unoccupied molecular orbitals (LUMO). Furthermore, there is a negative correlation between the energy band gap (the difference between HOMO and LUMO) and the number of carbon atoms in fullerenes [17–20], indicating fullerene molecules with different structures can tune the electronic structures that can affect their catalytic performance. This section summarizes the DFT calculations that have been conducted on different kinds of pure, heteroatom-doped, and metal-encapsulated fullerenes, and discusses their theoretic electrocatalytic performances.

2.1. Therocial reaction mechanism of ORR, OER, and HER

Fullerenes are potential candidates as electrocatalysts for ORR, OER, and HER as their pristine curvature and pentagon defect. The crucial parameter to evaluate the ORR, OER and HER character is the adsorption energy (E_{ads}) of the reaction intermediate species, which contributes to the investigation of the reaction mechanism and catalytic activity. Electrochemical reactions taking place in different solutions depend on different processes [21–25].

The Gibbs free energy (ΔG) of ORR, OER, and HER was calculated using the following equation based on Norskov et al.'s method [26].

$$\Delta G = \Delta E + \Delta ZPE - T\Delta S + \Delta G_U + \Delta G_{pH}$$

where ΔE, ΔZPE, and ΔS represent the energy difference of products and reactants, zero-point energy, and entropy, respectively.

$\Delta G_U = eU$, U is the electrode voltage vs. SCE. e is the charge transfer during the reaction. $\Delta G_{pH} = k_B T \ln 10 \times pH$, k_B and T represent the Boltzmann constant and the temperature, respectively.

The Gibbs free energy curves in ORR, OER and HER process are powerful parameters to characterize the reaction process, which is given in most DFT calculations.

2.2. Heteroatom-doped fullerenes

Heteroatom doping of fullerenes is an effective method to govern the electronic states and promote conductivity on the atomic scale, by which the electrocatalytic performance can be regulated [27,28]. For example, the prevailing N doping can activate the conjugated π configuration to create an active site for ORR by changing lone-pair electrons. N-doped fullerenes have been confirmed with superior electrocatalytic activities than intrinsic fullerenes [29]. Some similar results also reported that nitrogen-doped C_{60} ($C_{59}N$) displayed superior ORR activities to other heteroatom-doped C_{60} [28,30]. The investigation in Zhao's study indicated that O_2 molecules are favorably activated by $C_{59}B$ both kinetically and thermodynamically by generating two low-barrier intermediates [31]. Up to now, heteroatoms, including N, B, S, O, Si, and P, doped fullerene (C_{60}) have come into the sight of researchers due to the varying electronic characteristics induced by the heteroatoms. C_{60} as the most abundant portion among the fullerene family available for electrocatalysts is first discussed here [30,31].

To further throw light upon the effects of heteroatom-doped fullerene (HDF) on ORR, HDF has been systematically studied as a potential electrocatalyst for ORR [30]. The heteroatoms with different atomic radii, when doped into the cage of C_{60}, the size of which lead to different structure deformations [30]. Compared to the N and B atoms, Si, P, and S have large radii, which can result in large structure deformation. That implies more energy is necessary to construct $C_{59}Si$ and $C_{59}S$. The structural stability of doped fullerenes with different heteroatoms follows $C_{59}N > C_{59}B > C_{59}P > C_{59}Si > C_{59}S$ (Table 1). This variation in formation energy (E_f) can be attributed to the different sizes and electronegativities of the doped heteroatoms. The negative E_f values indicate that the composite materials are thermodynamically stable [32]. Meanwhile, the charge redistribution was also regulated by the doped heteroatoms. For the case of C_{60}, the charge redistribution is changed by introducing the heteroatoms with different electronegativity (Fig. 1), resulting in carbon atoms on the fullerene cage being positively charged, which is more advantageous for O_2 adsorption [31]. In addition, based on the E_{ads} in Table 1, the different E_{ads} between intermediate products and $C_{59}X$ indicate the differentiated electrochemical activity.

Different from C_{60} with 60 equal carbon atoms, there are five different types of carbon atoms (denoted as C_n, $n = 1$–5) in C_{70} molecular, Fig. 2a. Doping B, N, and Si in C_n sites of C_{70} (Denoted as X (C_n)) results in different formation energy (E_f) compare to the doping in C_{60} (Fig. 2b), which leads to different stability and charge redistribution of this doped fullerene (Fig. 2c) [30,32]. In addition, the ΔG_{*OH} shows a good linear relationship with ΔG_{*OOH} and ΔG_{*O} for the B, N, and Si-doped C_{70} (Fig. 2d), which is also displayed in other metals [33] or heteroatoms doped C_{60} [30] calculations. It is worth noting that N(C3) exhibits the lowest ORR overpotential (η^{ORR}) value of 0.67 V, while N(C4) exhibits the lowest OER overpotential (η^{OER}) value of 0.55 V, which demonstrates the best oxygen reduction activity and oxygen evolution activity, respectively. According to the calculated η^{ORR} and η^{OER}, it can be also known that doping heteroatoms are not always beneficial for the ORR and OER activity. Thus, rational heteroatoms doping is vital for designing and discovering new type of carbon-based electrocatalysts.

In addition to the nonmetallic doping, the metallic doped C_{60} ($C_{58}M$, M = Fe, Co, Ni, Mn, and Cu), in which metal atoms are used to replace the carbon atoms on the C_{60} cage, is studied by calculating the binding energies of ORR intermediate products [34]. The binding energy of $C_{58}Co$ is comparable to the idea Pt (111) lattice plane, and the detailed ORR path is given in Fig. 3a–f. The vital O_2 hydrogenation during the ORR process is downhill for $C_{58}Fe$, $C_{58}Co$, $C_{58}Ni$, and $C_{58}Mn$ except for $C_{58}Cu$, and *O reduced to *OH process on $C_{58}Mn$ is uphill, manifesting the

Table 1
Formation energy ($E_{formation}$) and adsorption energies (E_{ads}, eV) of ORR intermediate. Reprinted with permission from Ref. [30]. Copyright (2017) Elsevier.

Species	$E_{formation}$	O_2	OOH	O	OH
C_{60}	0	0.09	−1.58	−3.81	−6.11
$C_{59}N$	−6.56	−0.37	−2.57	−4.39	−6.20
$C_{59}P$	−3.55	0.08	−3.13	−2.67	−7.54
$C_{59}Si$	−3.15	−1.26	−4.66	−5.50	−7.41
$C_{59}B$	−4.82	−0.11	−2.23	−3.40	−7.78
$C_{59}S$	−1.90	−0.12	−2.07	−3.44	−7.72

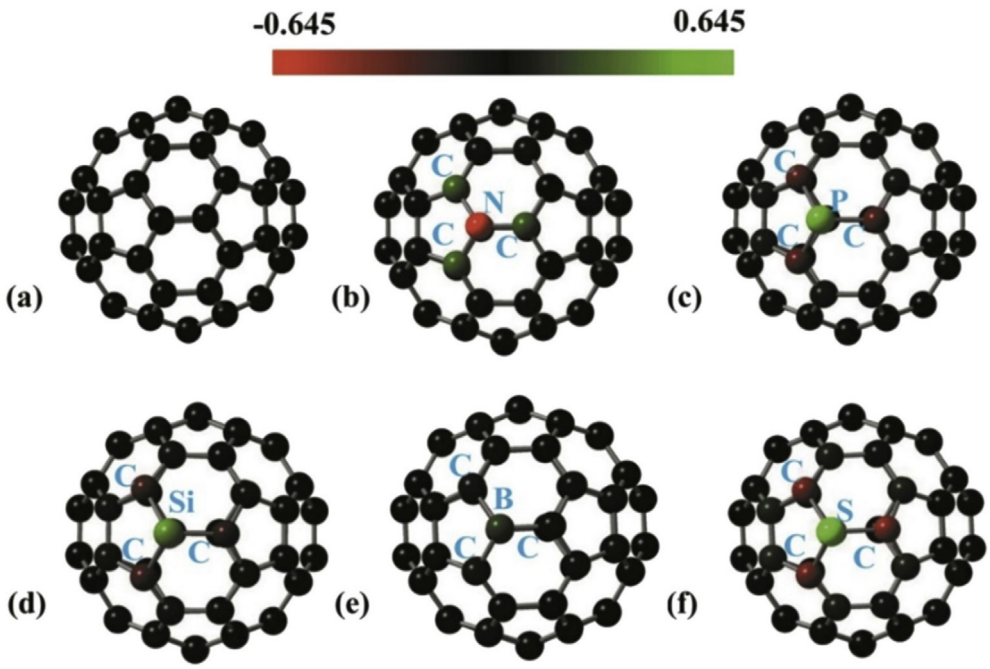

Fig. 1. Mulliken charge distribution on (a) C_{60}, (b) $C_{59}N$, (c) $C_{59}P$, (d) $C_{59}Si$, (e) $C_{59}B$ and (f) $C_{59}S$. Reprinted with permission from Ref. [30]. Copyright (2017) Elsevier.

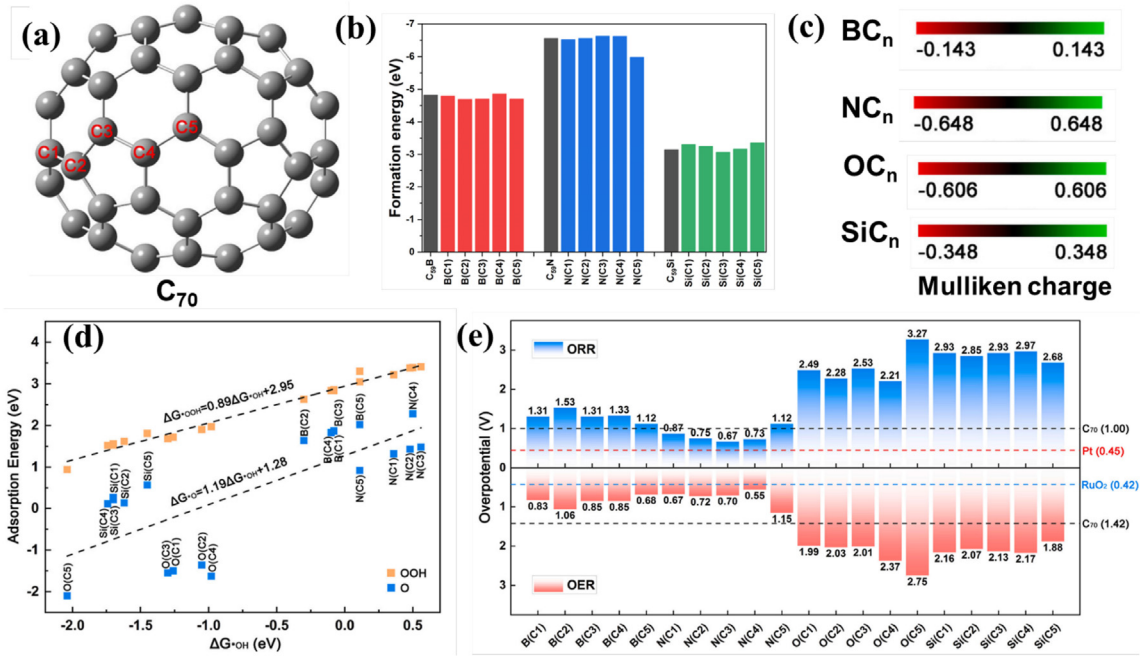

Fig. 2. (a) The C_{70} structure contains five types of carbon atoms. (b) The formation energy of $C_{59}X$ and X (C_n) (X = B, N, and Si). (c) Mulliken charge distribution on X (C_n), X represents B, N, O or Si, n = 1–5. (d) Relationship between the adsorption energy and ΔG_{*OH} on X (C_n). (e) The overpotentials of X (C_n) for oxygen reduction and oxygen evolution. Reprinted with permission from Ref. [32]. Copyright (2022) Elsevier.

thermodynamically unfavorable process for $C_{58}Cu$ and $C_{58}Mn$. The different downhill characteristics (i.e., different free energy changes) of the energy curves in Fig. 3a–e proved the different catalytic activity of the $C_{58}M$.

Another interesting doping mode is a hybrid of metal-nonmetal doped fullerenes, which is a kind of catalyst consisting of transition metal M and heteroatom N_4 co-doped in vacancy fullerene. Lots of experimental and theoretical studies have proven the metal center in M−N_4 is the reaction site of ORR [35–38]. In terms of the M−N_4 site doped fullerene (M-N_4-C_{64}, M = Fe, Co, and Ni), as shown in Fig. 3g–i, the Mulliken charges indicate nitrogen atoms in M-N_4-C_{64} and adjacent carbon atoms display negative charge density and positive charge density, respectively, which is attributed to the greater electronegativity of N atoms than that of C atoms. And the corresponding Mulliken charges of the Fe, Co, and Ni atoms were calculated as 0.664, 0.483, and 0.540|e|, respectively, suggesting the largest electron transfer from the metal center to N_4–C_{64} among the three samples. The positively charged site is more profitable for O_2 adsorption, thus the metal center was chosen as the reaction site

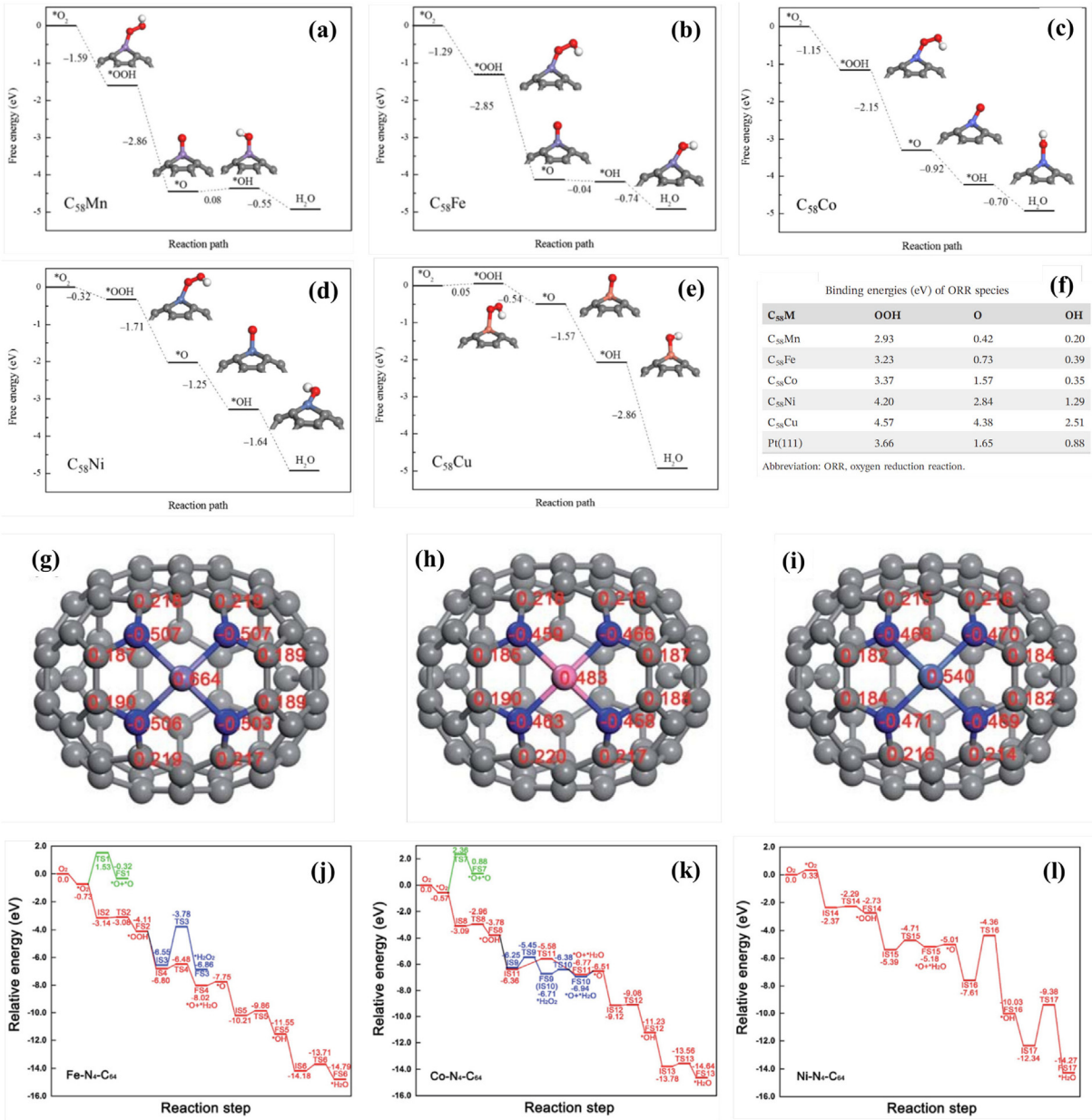

Fig. 3. (a–e) The calculated free energy curves of ORR on $C_{58}M$. (f) Binding energies of ORR. Reprinted with permission from Ref. [34]. Copyright (2019) Wiley-VCH GmbH. Charge distributions on (g) Fe–N_4–C_{64}, (h) Co–N_4–C_{64}, and (i) Ni–N_4–C_{64}. Relative energy curves for the ORR pathways on (j) Fe–N_4–C_{64}, (k) Co–N_4–C_{64}, and (l) Ni–N_4–C_{64}. Reprinted with permission from Ref. [38]. Copyright (2021) Royal Society of Chemistry.

for ORR. The relative energy curves intuitively revealed that the whole reaction energy variation during ORR paths of Fe–N_4–C_{64} and Co–N_4–C_{64} is degressive, which is conducive to positive-going reactions, demonstrating Fe–N_4–C_{64} and Co–N_4–C_{64} are high-efficiency ORR electrocatalysts [38].

2.3. Metal-encapsulated fullerenes

Different from the heteroatoms doped fullerene that heteroatoms are linked directly to the adjacent carbon atoms, endohedral fullerenes (EMFs, M@ fullerenes) contain encapsulated metal atoms with stable structure, where the encapsulated metal atoms are not directly linked to the adjacent carbon atoms. The active site for electrocatalytic reactions of EMFs depends on the redistribution of charge on a carbon cage. Lai et al. systematically studied the oxygen reduction catalytic performance of Mn@C_{60} (M = Mn, Co, Ni, Cu; n = 2–5). Taking Mn$_n$@C_{60} as an example, the inside Mn$_n$ cluster greatly regulates the charge states of carbon atoms on the C_{60} cage (Fig. 4a). The carbon atoms on the C_{60} cage are more negatively charged when more metallic atoms are encapsulated. The reaction species including OOH, O, and OH are adsorbed on the carbon atoms of the C_{60} cage, rather than the metallic cluster inside. The E_{ads} (OOH) and E_{ads}(O) as a function of E_{ads} (OH) were plotted on all the EMFs to descript the ORR activity (Fig. 4b), which displays slightly linear relationships between E_{ads} (OOH), E_{ads}(O) and E_{ads} (OH). Such results indicate E_{ads} (OH) is a vital parameter to assess the electrocatalytic performance of EMFs (Fig. 4c). More importantly, an activity volcano can be plotted using the calculated U_{rev} (reversible potential) rate-determining step (RDS). One can clearly see that the species located in Part I-III have different E_{ads} (OH), indicating the varying adsorbed energy with *OH. While the E_{ads} (OH) located in Part-II is moderated and beneficial to the ORR performance. Thus, Mn$_5$@C_{60} at the top of the volcano curve has the largest U_{rev} of 0.71 V and performs the highest ORR activities [39]. Similarly, to further explore the theoretical ORR activity of M$_x$@C_{60}, Nanjun Lai et al.'s work indicated Fe$_3$@C_{60} has a higher U_{rev} of 0.73 V

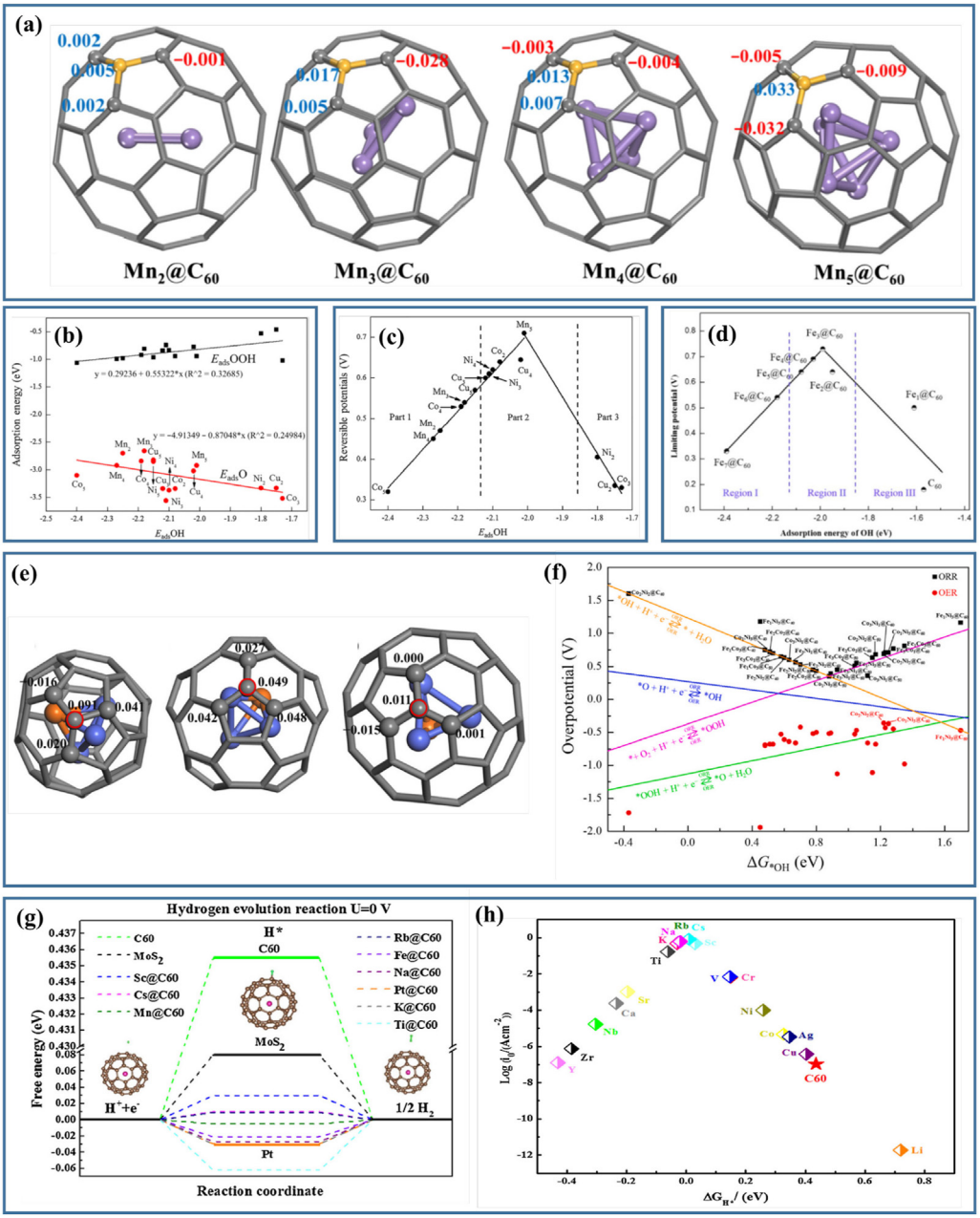

Fig. 4. (a) Charge distributions on Mn_2C_{60}, Mn_3C_{60}, Mn_4C_{60}, and Mn_5C_{60}. (b) Relationship between adsorption and $E_{asd}OH$ of ORR $M_n@C_{60}$. (c) Active volcano map of $M_n@C_{60}$. Reprinted with permission from Ref. [39]. Copyright (2020) Springer Nature. (d) Active volcano map of $Fe_x@C_{60}$. Reprinted with permission from Ref. [40]. Copyright (2020) IOP Publishing. (e) Charge distributions on $Co_3Ni_1@C_{40}$, $Co_3Ni_1@C_{50,s}$ and $Co_3Ni_1@C_{60}$. (f) Volcano plot of η^{ORR} and $-\eta^{OER}$ as a function of ΔG_{*OH}. (g) The calculated Gibbs free-energy diagram of HER under different reaction coordinate for $M@C_{60}$ catalysts. (h) Volcano curve of exchange current (i_0) as a function of the ΔG_{*H} for various metal atoms encapsulated in C_{60}. Reprinted with permission from Ref. [41]. Copyright (2017) Elsevier.

than $Mn_5@C_{60}$ (0.71 V) and Fe_x ($x = 0, 1, 2, 4, 5, 6$ and 7)$@C_{60}$ (Fig. 4d) due to improved energy gaps between HOMO and LUMO [40].

In addition to the monometallic cluster encapsulated in fullerene, a DFT study about bimetallic alloys encapsulated in fullerenes $M1_xM2_{4-x}@C_n$ ($M1_xM2_{4-x}$ represents Fe_xCo_{4-x}, Fe_xNi_{4-x}, Co_xNi_{4-x}; $x = 1, 2, 3$; $n = 40, 50, 60$) (Fig. 4e) revealed that more evident charge transfer between the bimetallic alloy core and the fullerene cage appears when the fullerene cage size decreases, which results in enhanced binding strength of the reaction species on the surface of $M1_xM2_{4-x}@C_n$ (Fig. 4e). The calculations verified that $Co_1Ni_3@C_{50}$ and $Co_2Ni_2@C_{60}$ are confirmed with the best oxygen reduction activity with $\eta^{ORR} = 0.35$ V and the best oxygen evolution activity with $\eta^{OER} = 0.36$ V, respectively (Fig. 4f). The results calculated above indicate not only the metal encapsulated but also the fullerene size has an effect on its ORR activity.

EMFs also exhibit HER performance theoretically. Aijun Du reported the potential HER application of $M@C_{60}$ (M = Na, K, Rb, Cs, Sc, Ti, Mn, and Fe) using the DFT calculations and pointed out that the size of encapsulated atoms plays a crucial role in the HER performance of EMFs [41]. As shown in Fig. 4g, compared to the C_{60}, the values of ΔG_{*H} for $M@C_{60}$ approaching zero manifests the enhanced HER activity. Known from the volcano curve in Fig. 4h, a negative ΔG_{*H} impedes the desorption of H and a positive ΔG_{*H} restricts the adsorption of H during the HER process. $Rb@C_{60}$ with the ideal ΔG_{*H} value close to zero exhibits the highest HER activity. While the $Li@C_{60}$ with Li atom encapsulation (Li atom has a smaller size than Rb) performs the worst HER activity. By introducing the metal atoms into the EMFs, Adedapo S. Adeyinka et al. found the molybdenum-encapsulated, iron-doped, and gold-decorated composite ($AuFeMo@C_{24}$) can be also performed to catalyze the hydrogen evolution reaction [42].

3. Experimental application

Based on the deep insight gained from studying potential ORR, OER, and HER activity of fullerene and its derivates, experimental explorations have been carried out to confirm some of the DFT calculations. DFT calculations have shown that heteroatom doping and metal/non-meta

encapsulated fullerenes can greatly enhance the electrocatalytic activity by tuning the electronic structure and adsorption energy between the active sites and intermediates. For practical applications of fullerene in ORR, OER, and HER, they are commonly used as feedstock to prepare fullerene-based composite, self-assembled crystals, EMFs, and derivatives.

3.1. Fullerene-based composites

Using fullerenes to construct fullerene-based composites is a widely studied field because the composites can take advantage of both components and achieve a synergistic catalytic effect. The ultra-small molecular diameter of zero-dimensional fullerene renders it an ideal candidate for supporting or adsorbing onto a particular base, such as the carbon nanotubes (CNTs), sulfides, metals, and oxides, through noncovalent interactions, such as π–π interactions and van Der Waals force, and covalent bonding [1,11–14,43–47]. Once composited with these substrates, fullerene molecules can extract electrons from the surrounding substrate because of their strong electron acceptor properties, resulting in the tuned electronic structure of the adjacent substrates [48].

3.1.1. Fullerene/carbon composites

The use of 1D CNTs in electrocatalyst applications has received considerable attention due to their excellent conductivity and chemical stability [49]. However, the limited number of active sites on pristine CNTs restricts their activity when used directly as an electrocatalyst. Surface self-activation or introduction of the active component is crucial to the catalytic performance. While the C_{60} molecule, with all sp^2-hybridized carbon atoms and incomparable electron affinity, has high catalytic activity, however, the conductivity of which is extremely poor. A combination of C_{60} with CNTs was designed by Dai and co-workers, where the quantized C_{60} molecules were adsorbed on the surface of CNTs via noncovalent interaction as shown in Fig. 5a [1]. The process of adsorbing C_{60} onto SWCNTs involved suspending SiO_2/Si wafers with SWCNTs in de-ionized water via ultrasonication, along with C_{60} with a concentration of 1.96 mol L^{-1} for 5, 10, 15, and 20 min (denoted as C_{60}-SWCNTn, $n = 5$, 10, 15, and 20 min). One can clearly see the C_{60} was adsorbed on the surface of SWCNT (Fig. 5b). The C 1s peak shift in XPS verified the electrons are transferred from SWCNTs to C_{60} (Fig. 5c). The results indicated that the distinct interfacial charge transfer between C_{60} and CNTs leads to the remarkable electrocatalytic performance of SWCNT15 and substantially low overpotentials in oxygen reduction

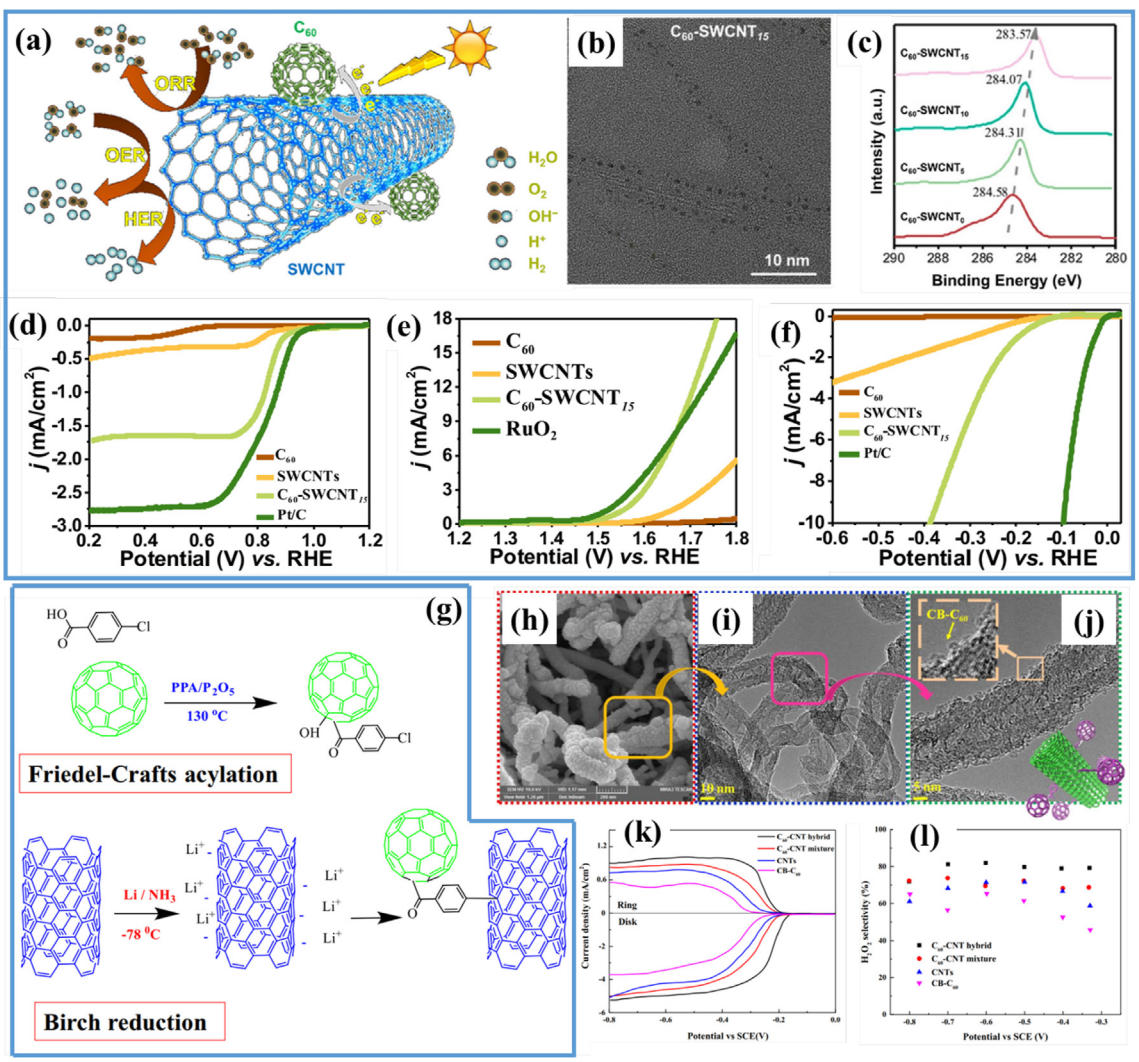

Fig. 5. (a) Illustration of the charge transfer process between C_{60} and SWCNT. (b) TEM images and (c) C 1s XPS spectra of C_{60}-SWCNTn ($n = 0$, 5, 10, and 15 min). LSV curves of (d) ORR, (e) OER, and (f) HER for C_{60}-SWCNTn and Pt/C in 0.1 mol L^{-1} KOH. Reprinted with permission from Ref. [1]. Copyright (2019) American Chemical Society. (g) Procedure of CB-C_{60} and C_{60}-CNT hybrid. (h) SEM and (i, j) TEM images of C_{60}-CNT hybrid. (k) LSV and (l) H_2O_2 selectivity of the C_{60}-CNT hybrid, C_{60}-CNT mixture, CNTs, and CB-C_{60} at 1600 rpm in O_2-saturated 0.05 mol L^{-1} H_2SO_4 solution with a scan rate of 10 mV s^{-1}. Reprinted with permission from Ref. [44]. Copyright (2019) Springer Nature.

(Fig. 5d), oxygen evolution (Fig. 5e), and hydrogen evolution (Fig. 5f) compared to pristine CNTs and C_{60}. Additionally, the SWCNT15 exhibited a similar current decrease as the commercial Pt/C and RuO_2 electrocatalysts, indicating unprecedented long-term stability towards ORR, OER, and HER. Furthermore, Zhang et al. explored a novel C_{60}-CNT hybrid leveraging the direct covalent linkage of C_{60} derivative molecules with CNTs sidewalls (Fig. 5g) [44]. As shown in the SEM and HR-TEM image of the C_{60}-CNT hybrid in Fig. 5h–j, spherical C_{60} molecules are covalently conjugated on the CNTs sidewall, and individual size of C_{60} spheres was found to be around 1 nm. Compared to CNTs and CB-C_{60}, the C_{60}-CNT hybrid showed a higher ring/disc current, higher catalytic activity, and higher H_2O_2 selectivity (Fig. 5k–l), which further indicated the direct covalent linkage of C_{60} and CNT can effectively enhance the catalytic activity. And the C_{60}-CNT hybrid electrode can keep a stable current over 10 h under a selected potential of −0.2 V vs. SCE, demonstrating the stable production of H_2O_2.

Furthermore, C_{60} can be loaded on doped graphene and graphitic carbon flakes to modify the electrocatalytic performance. Michal Otyepka and colleagues also found that the durability and electrocatalytic performance of a non-metal covalent hybrid of fullerene and F-doped graphene for HER was improved due to the inter-hybrid charge-transfer phenomena resulting from the electron-accepting properties of C_{60} and the high conductivity and large surface area of graphene [50]. Interestingly, Juan C. Noveron et al. synthesized fullerene (C_{60}) inserted boron carbon nitride nanosheet (F/BCN) [2]. Briefly, a fullerene solution in toluene (ranging from 5 to 30 wt %) was added to 20 mL of IPA containing 50 mg of BCN NSs powder. The resulting mixture was then bath sonicated for 30 min to form the F/BCN nanohybrids, as shown in Fig. 6a. STEM images of the 10% F/BCN nanohybrids, presented in Fig. 6b, reveal that C_{60} molecules are uniformly distributed on the surface, with sizes of approximately 0.9 nm. The peak locations of high-resolution C 1s XPS spectra for F/BCN hybrids gradually negatively shifted to some content when C_{60} was introduced into F/BCN hybrids, which can be explained by electron transfer from the BCN NSs to C_{60}.0.5 eV (284.63–284.33 eV) peak shift of C 1s is found in 10% F/BCN hybrid, which is higher than that of the other samples, indicating the more pronounced charge transfer in the 10% F/BCN hybrid. A more pronounced charge transfer in the 10% F/BCN hybrid confirmed by the largest binding energy shifting of 0.5 eV (284.63–284.33 eV) than others implies the great potential in enhancing the electrocatalytic activity [1]. The HER onset potentials of the obtained nanohybrids are given in Fig. 6d, the value of 10% F/BCN is as low as −0.042 V vs. RHE which is much lower than the other samples. The top position of 10% F/BCN in the volcano plots indicates the most active catalytic rates. For the case of OER, 10% F/BCN also exhibits the lowest overpotential of 390 mV and is located on the top of the volcano plots, as shown in Fig. 6f–g. When applied for ORR, 10% F/BCN shows an E_{on} = 0.92 V, and an E_{half} = 0.79 V vs. RHE (Fig. 6h). Also, the top position on the volcano plots of 10% F/BCN indicates its superior catalytic performance (Fig. 6i). Moreover, even under a chronoamperometric measurement over 12 h, the current of 10% F/BCN do not show obvious attenuation, which confirms the hybridization between C_{60} and BCN can greatly improve the catalytic stability. These results indicate the hybridization of C_{60} and 2D doped graphene and graphitic carbon flakes is a promising strategy to develop new electrocatalysts.

3.1.2. Fullerene/sulfide composites

2D MoS_2 is a promising electrocatalyst, the edge sites of which are considered as catalytic sites for HER. However, the basal planes of MoS_2 have been confirmed to be catalytically inert, which greatly restricts its catalytic performance [51,52]. Furthermore, the semiconductive characters and low charge carrier mobility of MoS_2 indicate the pristine electronic properties of MoS_2 can be regulated by constructing a p-n heterojunction interface through hybridization with another semiconductive material [53]. C_{60} fullerene is another semiconductive material with strong electron affinity, which can greatly modulate the adjacent electron distribution of the contacted substrates. Chen and co-workers using VASP calculations found that the LUMO of MoS_2

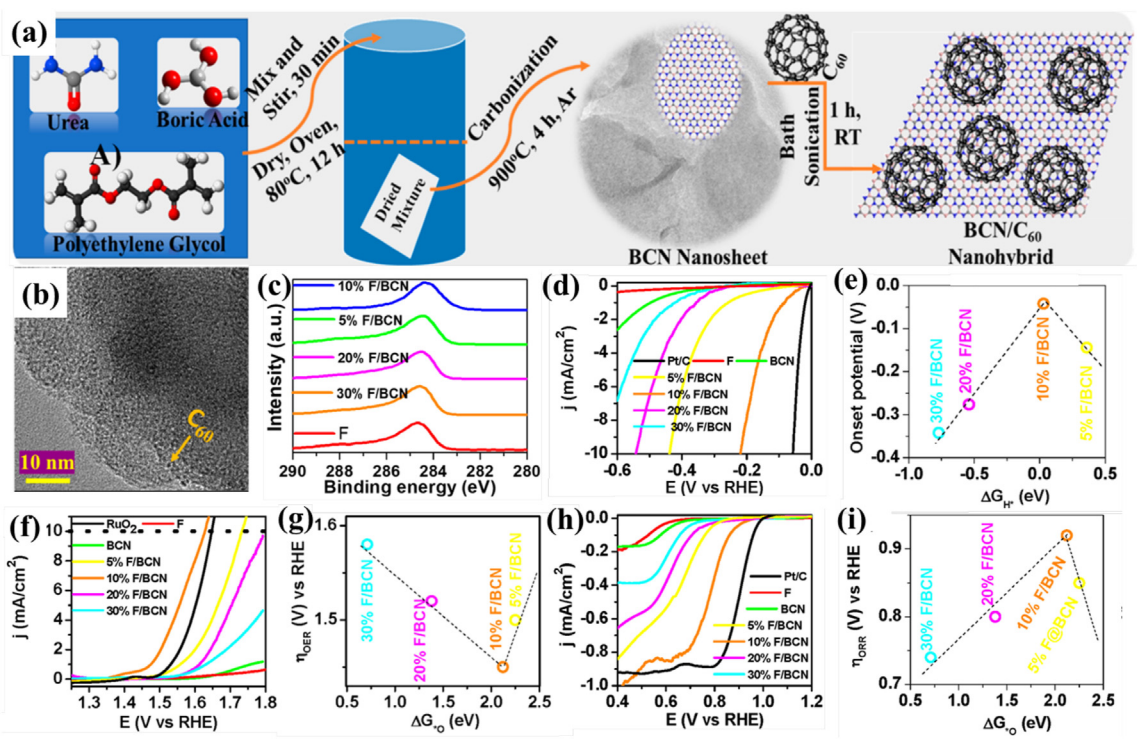

Fig. 6. (a) Illustration of the synthesis of F/BCN nanohybrids. (b) STEM images of 10% F/BCN, nanohybrids. (c) Comparison of C 1s spectra for F and *x*F/BCN nanohybrids (x = 5%, 10%, 20%, and 30%). (d) HER LSVs for F, *x*F/BCN, Pt/C and BCN in 0.5 M H_2SO_4. (e) Volcano plots of onset potential vs ΔG_{*H} for xF/BCN. (f) OER LSVs for F, *x*F/BCN, BCN and RuO_2 in 0.5 M NaOH. (g) The volcano curves of η^{OER} vs ΔG_{*O}. (h) ORR LSV curves of F, BCN, *x*F/BCN for ORR in 0.5 NaOH. (i) Volcano plots of η^{ORR} vs. ΔG_{*O}. F represents C_{60}. Reprinted with permission from Ref. [2]. Copyright (2021) American Chemical Society.

(−4.5 eV) is lower than that of C_{60} (−3.8 eV), leading to charge transfer and electron accumulation on MoS_2 when the two semiconductors are interfaced [53]. The electron redistribution at the MoS_2/C_{60} can create a built-in electric field that stabilizes the increasing electron density in MoS_2, further reduces the junction-barrier height, and allow facile electron tunneling and transport. This gives rise to conductive pathways along the MoS_2/C_{60} p−n heterojunctions [53].

Consequently, modulating the electronic structure of MoS_2 with C_{60} to enhance the electrocatalytic activity of MoS_2 is feasible. In early 2016, Sarbajit Banerjee et al. introduced C_{60} in varying concentrations to the surface of MoS_2 to construct C_{60}/MoS_2 composite. They found the optimal amount of C_{60} in MoS_2 can effectively lower the charge transfer resistance (Fig. 7a and b) and improve the HER catalytic activity, which revealed that the charge transfer from the nC_{60} clusters to MoS_2 can change the semiconductive charge state of MoS_2 and further enhance the HER performance (Fig. 7c) [12]. A study by Echegoyen explored the use of MoS_2/C_{60} composite as an HER catalyst via combining ultrasonication with an organic solvent-assisted strategy, see Fig. 7d, [47]. MoS_2/C_{60} composite with various C_{60} loadings exhibited HER overpotential lower than that of the pristine C_{60} and MoS_2. 1T-MoS_2/C_{60} heterostructure with 20 wt% of C_{60} shows the smallest overpotentials (highest HER activity) and excellent stability (Fig. 7e and f). Related DFT calculations provided further insight that the improved activity is from the anchoring of C_{60} on 1T-MoS_2. The optimized atomic model of C_{60} molecules stabilized on 1T-MoS_2 is given in Fig. 7g. One can clearly see that the electrons transfer from the C atoms of C_{60} at the interface to the in-plane MoS_2, which is in line with Chen's work discussed above. The density of states (DOSs) curves display the different waveforms, revealing the interaction between C and Mo/S atoms (Fig. 7i). The Gibbs free energy diagrams for 20 wt% 1T-MoS_2/C_{60} show a value of just −0.03 eV, further confirming its superior HER activity. In addition to MoS_2, fullerene can also be used as the regulating agent to modify the CeNdS (Forming CeNdS/C_{60}) [45]. Taisal Iqbal and co-workers found that the covered C_{60} over CeNdS provides strong interfacial interaction between CeNdS and C_{60}, resulting in a very small overpotential of 346 mV in a medium consisting of 1.0 M KOH.

3.1.3. Fullerene/LDH or metal composites

Fullerenes can be also used to regulate the metals and oxides-based materials via covalent bonding or non-covalent adsorption. We know that non-noble metal oxides and layered double hydroxides (LDHs) face significant challenges in achieving high electrocatalytic activity due to

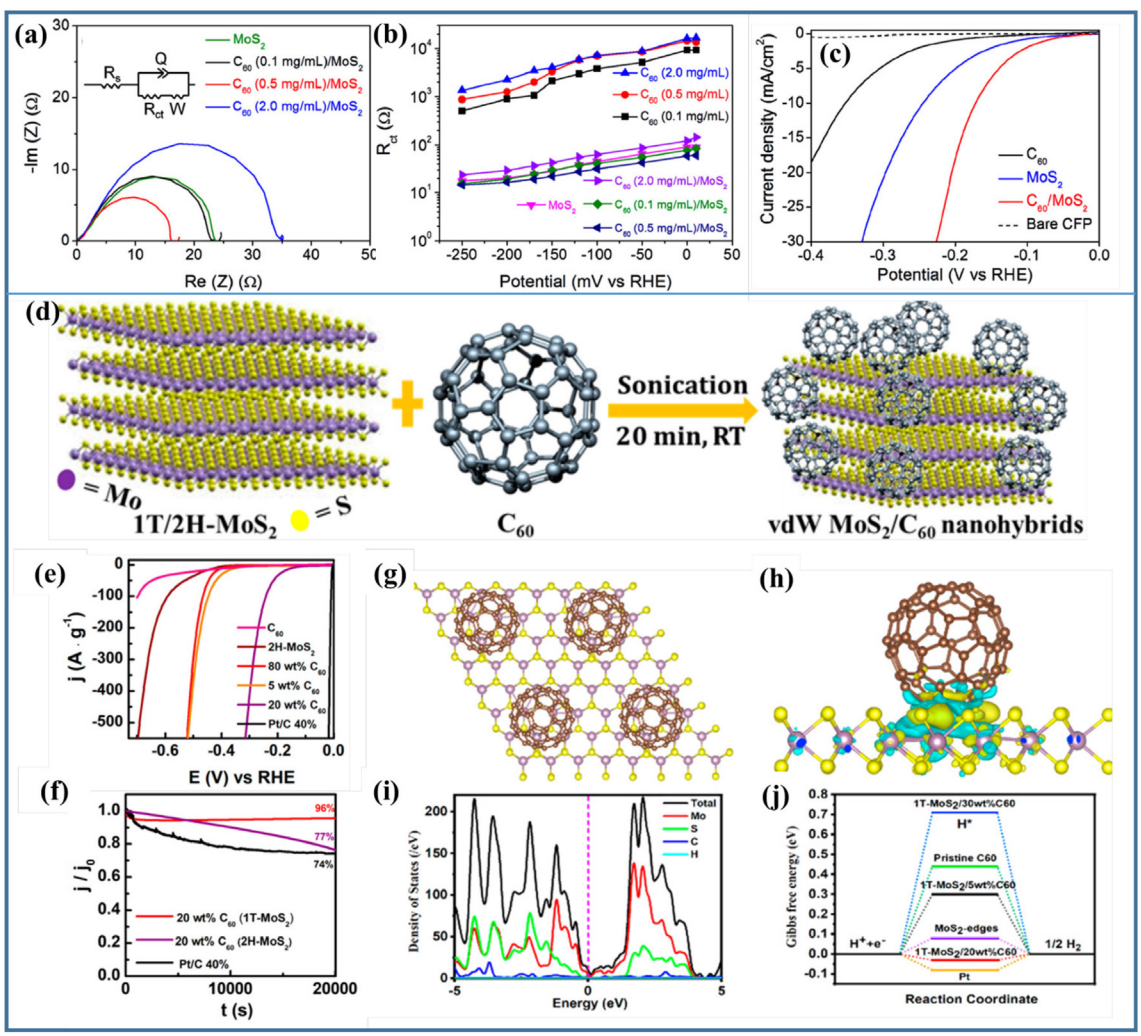

Fig. 7. (a–c) Nyquist plots and charge-transfer resistance (R_{ct}) of as-prepared 3D MoS_2 nanosheets and hybrid nC_{60}/MoS_2. Reprinted with permission from Ref. [12]. Copyright (2016) American Chemical Society. (d) The synthesis of the MoS_2/C_{60} composite. (e) Mass-normalized catalytic currents for C_{60}, 2H–MoS_2, commercial Pt/C 40%, and the 2H–MoS_2/C_{60} composite with 5, 20, and 80 wt% of C_{60} in 0.5 M H_2SO_4. (f) Stability curves of 2H–MoS_2/20 wt% C_{60} and 1T-MoS_2/20 wt% C_{60} at. (g) Optimized atomic model and (h) the calculated charge redistribution of 1T-MoS_2/C_{60} composite. Mo, S, and C atoms have been represented by violet, yellow, and brown spheres respectively. (i) DOSs of the MoS_2/20 wt% C_{60} composite. (j) Gibbs free energy curves of HER on different catalysts. Reprinted with permission from Ref. [47]. Copyright (2020) American Chemical Society.

their sparse catalytic edge site and poor electrical conductivity [43]. Quantized functional fullerenes can serve as an additive to increase the number of actives via insertion into the substrates. Additionally, the functional groups introduced into the fullerene cage can improve the conductivity and facilitate the charge transfer of LDHs. Chunru Wang and co-workers inserted HNO_3-functionalized C_{60} (fullerene quantum dot, FQD) into the interlamination of CoNi LDH, forming an atomic-scale sandwich-like structure (FQD/CoNi-LDH/NF electrode) [43]. As shown in Fig. 8a, the HNO_3 treatment of C_{60} introduced sufficient nitrogen and oxygen functional groups, for example, $–NH_2$, –OH, and –COOH groups, which improve the conductivity and facilitates the charge transfer of LDH. FQD/CoNi-LDH/NF electrode exhibited the smallest charge transport resistance (R_{ct}) among the tested samples, as shown in Fig. 8b, d, and demonstrated enhanced OER and HER overpotential of $\eta 30 = 320$ mV

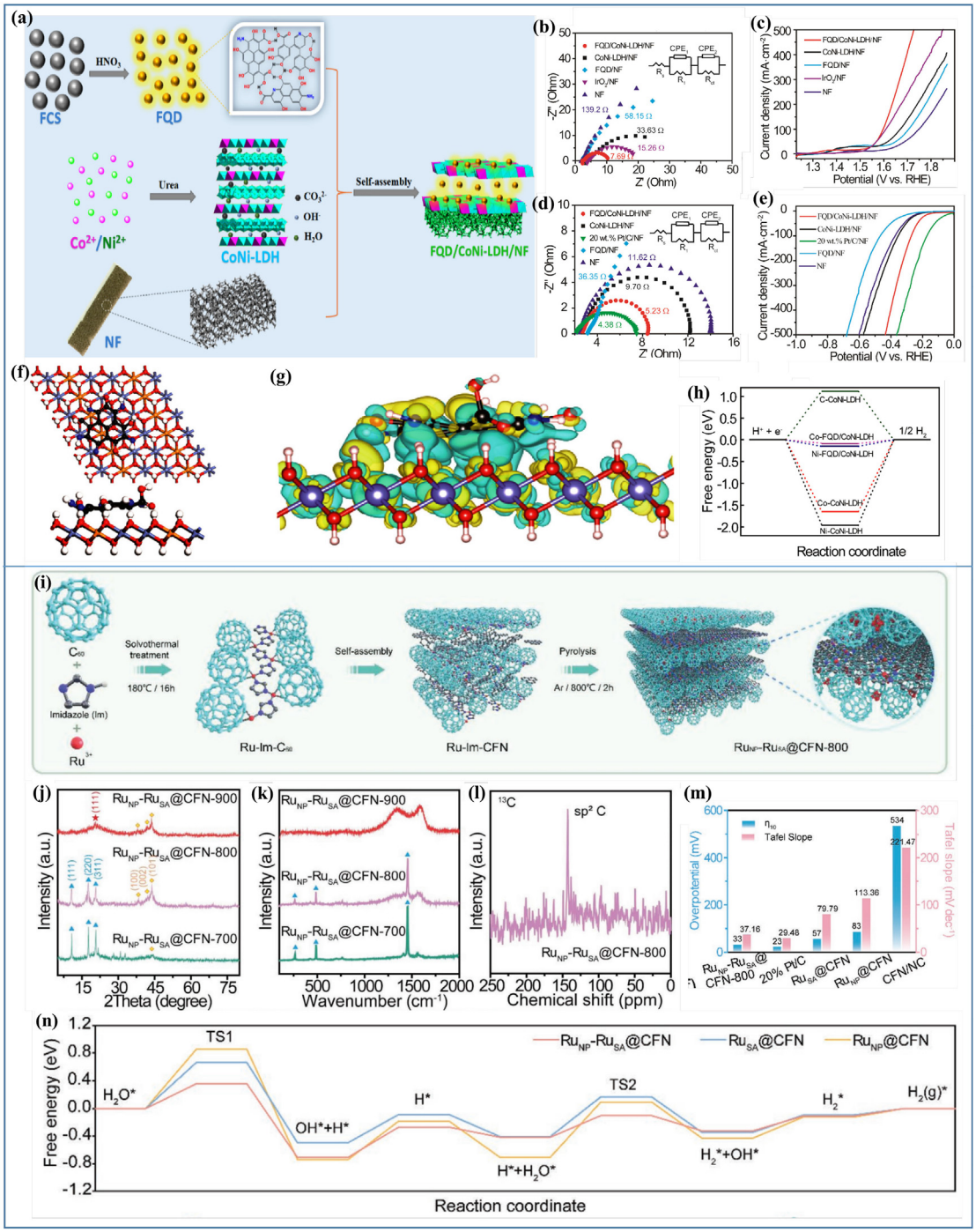

Fig. 8. (a) Illustration preparation of FQD/CoNi-LDH/NF. OER performance: (b) Nyquist plots and (c) LSV curves of FQD/CoNi-LDH/NF in 0.1 M KOH. HER performance: (d) Nyquist plots and (e) LSV curves of FQD/CoNi-LDH/NF in 0.1 M KOH. (f) The optimized model of FQD/CoNi-LDH. (g) Calculated charge-density difference of the FQD/CoNi-LDH model. The iso-surface value of the color region is 0.01 e $Å^{-3}$. (h) Free energy diagram of the HER on CoNi-LDH and FQD/CoNi-LDH. The different H adsorption sites on CoNi-LDH and FQD/CoNi-LDH are denoted by C, Co, and Ni. Co: yellow, Ni: light blue, H: white, C: black, O: red, N: blue. Reprinted with permission from Ref. [43]. Copyright (2020)Elsevier. (i) Illustration of the synthetic process of RuNP-RuSA@CFN-800. (j) XRD patterns and (k) Raman spectrum of RuNP-RuSA@CFN-X ($X = 700$, 800, and 900). (l) Solid–state ^{13}C NMR of RuNP-RuSA@CFN-800. (m) Comparison of the $\eta 10$ and Tafel plots for RuNP-RuSA@CFN-800, RuSA@CFN, RuNP@CFN, CFN/NC, and 20% Pt/C in 1 M KOH solution. (n) Free energy of HER on RuNP-RuSA@CFN, RuSA@CFN, and RuNP@ CFN. Reprinted with permission from Ref. [14]. Copyright (2023) Wiley-VCH GmbH.

and $\eta 10 = 150$ mV, respectively. DFT calculations were then performed with an optimized model in Fig. 8f. The Bader charge analysis confirmed the charge transfer from FQD to CoNi-LDH (Fig. 8g). Furthermore, the formation of FQD/CoNi-LDH greatly improves the Gibbs free energy values ΔG_{*H} from −1.65 to −0.09 eV and from −1.96 to −0.15 eV for the adsorption on Co and Ni sites, respectively, indicating the enhanced catalytic activity of FQD/CoNi-LDH compared to the pristine CoNi-LDH (Fig. 8h).

Similarly, when hybridizing fullerene with metal, the charge distribution around the metal nano-particle and single metal atoms can be also regulated by the adjacent fullerene. Yongqiang Feng and co-workers assembled a repeating layer-by-layer configuration of C_{60}/Ru/C60/Ru via covalent bonding, and the RuNP-RuSA@CFN-800 sample was obtained after annealing the assembled precursor at 800 °C, as shown in Fig. 8i, [14]. The major peaks at 10.8°, 17.7°, and 20.8° were assigned to the (111), (220), and (311) planes of the fcc crystal structure of C_{60}, and the peaks at around 44.9°, 49.4°, and 51.6° can be attributed to the (100), (002), and (101)planes of hexagonal Ru, which confirmed the fullerene substance remains stable even at high temperature of 800 °C. The prominent peaks at 275.4, 492.1, and 1466.2 cm^{-1} in the Raman spectra and solid-state ^{13}C NMR represent C═C stretching and sp^2 carbon of C_{60}, respectively, further confirming the existence of C_{60} in RuNP-RuSA@CFN-800 (Fig. 8j–l) [48,54,55]. RuNP-RuSA@CFN-800 exhibited the lowest HER overpotential of $\eta 10 = 33$ mV and a tafel slope of 31.76 mV dec^{-1}. The DFT calculations revealed the ΔG_{*H} values for RuSA@CFN, RuNP-RuSA@CFN, and RuNP@CFN are −0.09, −0.27, and −0.37 eV, respectively. ΔG_{*H} alone is the only factor that can be used to describe the HER activity due to the large energy barrier of water dissociation [56]. The kinetics of water dissociation for RuNP-RuSA@CFN, RuSA@CFN, and RuNP@CFN was compared, and it was found that the transition state (TS) barrier for water dissociation was significantly lower for RuNP-RuSA@CFN, with a value of 0.36 eV, as compared to RuSA@CFN (0.57 eV) and RuNP@CFN (0.85 eV). Under the circumstances, RuNP-RuSA@CFN performed a favorable reaction kinetics. Other research groups have also studied the C_{60}@Cu/Cu-oxide for ORR [13], MnOx@C_{60} for OER [11], and NiO/C_{60} composites for OER

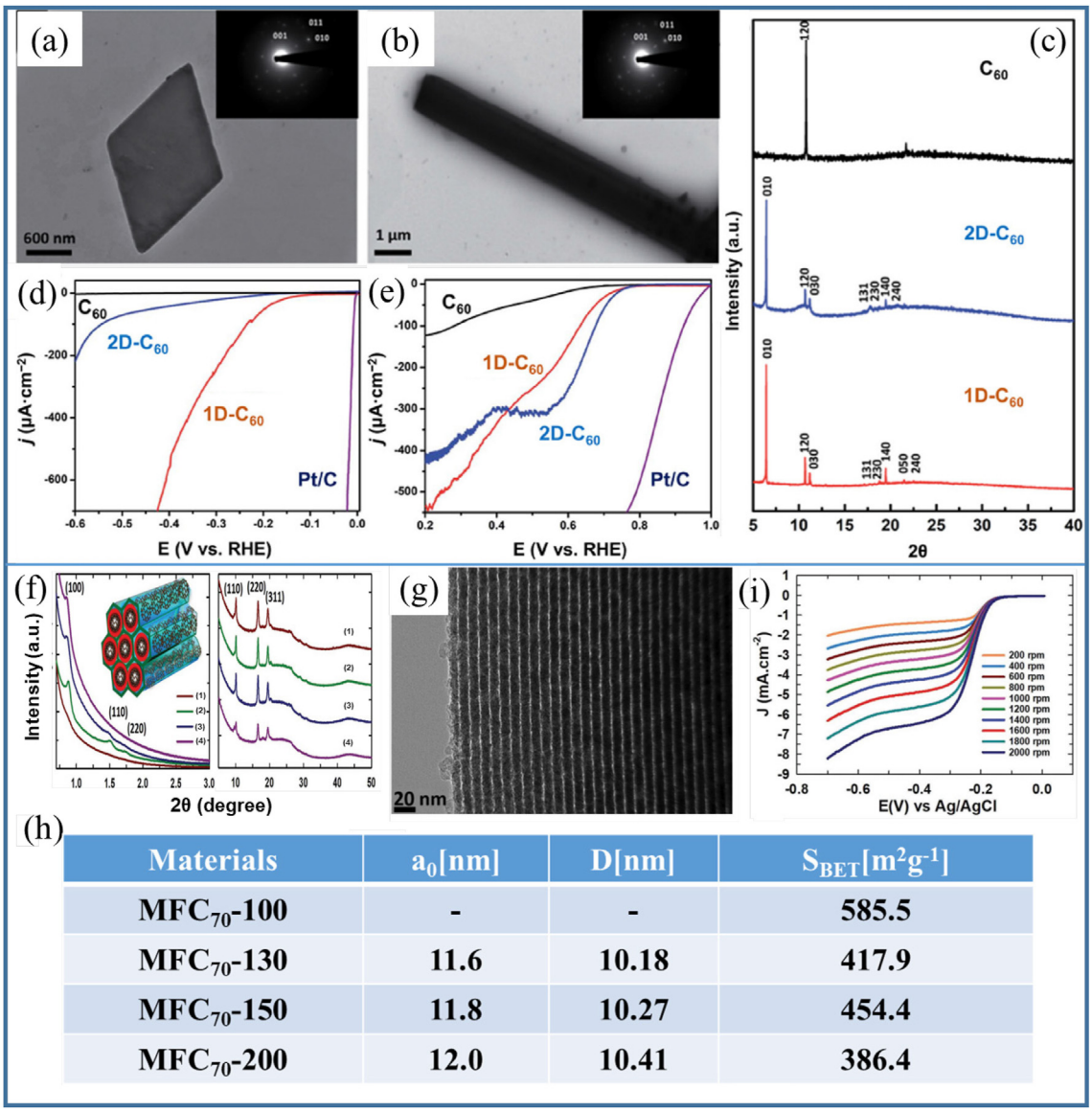

(h)

Materials	a_0[nm]	D[nm]	S_{BET}[m^2g^{-1}]
MFC_{70}-100	-	-	585.5
MFC_{70}-130	11.6	10.18	417.9
MFC_{70}-150	11.8	10.27	454.4
MFC_{70}-200	12.0	10.41	386.4

Fig. 9. TEM of (a) C_{60} nanoflakes and (b) C_{60} nanotubes, (c) XRD of C_{60} nanoflakes and C_{60} nanotubes. (d) HER LSVs curves of C_{60}, C_{60} nanoflakes, and C_{60} nanotubes in 0.5 M H_2SO_4 at 2 mV s^{-1}, (e) ORR LSV curves of C_{60}, C_{60} nanoflakes, and C_{60} nanotube at different rotation rates in 0.5 M NaOH 5 mV s^{-1}. Reprinted with permission from Ref. [63]. Copyright (2020) Royal Society of Chemistry. (f) XRD patterns of (1) MFC_{70}-100, (2) MFC_{70}-130, (3) MFC_{70}-150, and (4) MFC_{70}-200. (g) HRTEM image of MFC_{70}-150. (h) Structural character of MFC_{70}-T. (i) LSV curves of MFC_{70}-150 at 5 mV s^{-1}. Reprinted with permission from Ref. [70]. Copyright (2018) Wiley-VCH GmbH.

[46], and the results showed the universal enhancement properties of fullerene for electrocatalysis.

3.2. Fullerene molecules and their derivates

3.2.1. Fullerene crystals

The application for ORR, OER, and HER of pristine fullerene powder is retrained by its inferior electronic conductivity that impedes the charge transfer during the catalytic process. Fortunately, owing to the sphere-shaped molecular structures and adjustable architectures of fullerenes, it is found that constructing fullerenes into micro-structure using liquid-liquid interfacial precipitation (LLIP) is an effective method to overcome those limitations [15,57–62].

Luis Echegoyen and co-workers reported two types of fullerene micro-structure including C_{60}-based rhombic-shaped nanoflakes and nanotubes via an LLIP solvent engineering strategy, which were used as bifunctional water-splitting catalysts (Fig. 9a and b) [63]. In such work, *tert*-butyl alcohol and toluene were used as poor and good solvents, in which the C_{60} microstructure precipitated from the mixture solution after static settlement for 24 h. XRD in Fig. 9c demonstrated the distinguished crystal type of the C_{60} nanoflakes (2D-C_{60}), C_{60} nanotubes (1D-C_{60}), and pristine C_{60}. Typically, C_{60} crystal exhibited an hcp structure, which is in line with some previous works [64–67]. It can be clearly seen that new peaks located at around $2\theta = 6°$ that correspond to the (010) lattice plane is different from that of the pristine C_{60} ($2\theta = 10°$), which reveals the rearrangement of C_{60} molecules in the newly formed structure. Both the 1D and 2D-C_{60} structures exhibited lower overpotential for HER and high half-wave potential for ORR in Fig. 9d and e, solidly revealing that self-assembling of fullerenes via LLIP is an effective way to promote the electrocatalytic properties. Such results can be explained by a called "tip effect" of the curved interfaces caused by the different dimensionality [68,69].

An ordered micromorphology of the fullerene was further confirmed to have positive effects on its electro-catalytic properties [70]. Ajayan Vinu and co-workers constructed an ordered mesoporous C_{70} crystalline using an SBA-15 template. Just simply drop the C_{70} solution into the SBA-15 template at 100, 130, 150, and 200 °C, respectively, to form a fullerene–silica composite, then annealing the composites under N_2 atmosphere at 900 °C, the corresponding samples were named MFC$_{70}$-T (T = 100, 130, 150 and 200 °C). Interestingly, although the fullerene is easy to be carbonized and transformed into graphitic or amorphous carbon [36,71], the SBA-15 templated can effectively protect C_{70} from

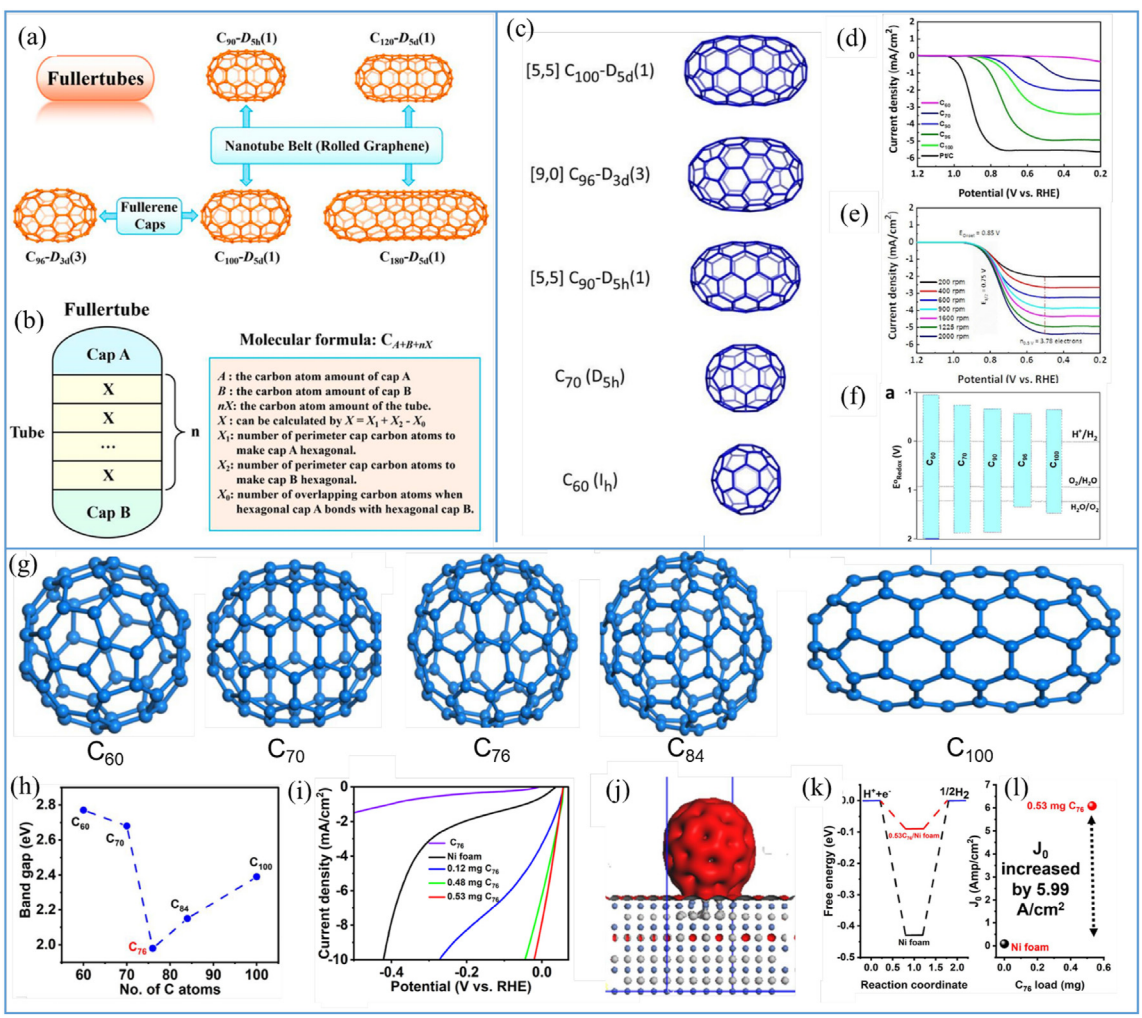

Fig. 10. (a) Illustration of pristine fullertubes and corresponding (b) molecular formula: CA + B + nX. Reprinted with permission from Ref. [75]. Copyright (2020) American Chemical Society. (c) Structure illustration, (d) ORR LSV curves at 1600 r min^{-1}, and (e) LSV plots of C_{96} in O_2-saturated 0.1 M KOH. (f) Mott Schottky analyses of the CA + B + nX. Reprinted with permission from Ref. [3]. Copyright (2022) Wiley-VCH GmbH. (g) Structures, (h) bandgap energies of C_{60}, C_{70}, C_{76}, C_{84}, and C_{100} fullerenes. (i) LSV curves of Ni foam and Ni foam with different C_{76} loading in 0.5 M H_2SO_4. (j) Isosurface of the electron density distribution with C_{76} loading (the isovalue is 0.1 e Å^{-3}). (k) Gibbs free energy changes (ΔG_{*H}) of H adsorption on Ni foam and C_{76}-coated Ni foam and (l) corresponding exchange current. Reprinted with permission from Ref. [79]. Copyright (2022) American Chemical Society.

being carbonized, thus maintaining the intrinsic C_{70} cage structure. As shown in Fig. 9f–h, MFC_{70}-T reflects a similar XRD pattern to the SBA-15 template, revealing the ordered mesopore structure can be perfectly duplicated with this strategy. Thus, the obtained MFC_{70}-150 displays the same 2D hexagonal lattice (P6mm) as the SBA-15 template and possesses an interplanar spacing over 10 nm. When used for ORR, the limiting current density of MFC_{70}-150 performs an analogous limiting current density to the 20% Pt/C [72]. The electron transfer number of MFC_{70}-150 is 3.6, higher than that of the MFC_{60} ($2e^-$), suggesting the better performance of MFC_{70} for $4e^-$ ORR. Such results indicate that the highly crystalline ordered mesoporous structure of C_{70} fullerene can greatly meliorate the oxygen reduction performance. Of course, the crystallinity and pore structure of nano-micro scaled fullerene crystals can be further tuned via high-temperature annealing, with which lots of carbons, including CNTs, heteroatom doped carbon et al., have been reported [6,36,73,74]. However, the intrinsic cage structure is severely destroyed and no fullerene anymore, thus the fullerene-derivated carbons are not discussed here.

3.2.2. Fullertubes

As discussed above, C_{60} and C_{70} with different sizes perform different electrocatalytic activities [70]. Here, the effects of different sizes of fullerenes on the electrocatalytic performance were intensely explored. For the case of fullerene with more carbon atoms, named higher fullerenes, the HOMO–LUMO gaps are generally reduced, which implies the promotion of the conductivity that is good for the efficient electron transfer, thus guaranteeing the positive effect on an electrocatalyst [7]. Revolutionary experimental research about the higher fullerenes is related to the extraction of fullertubes which is a new fullerene with 100–200 carbon atoms (denoted as C100–C200), see Fig. 10a and b [75]. Fullertubes are fundamentally assembled with rotated monolayer graphene and two half-fullerene end-caps and show a similar structure to SWCNT. According to the fullerene end-cap configuration, the molecular formula of a classic fullertube can be noted as $C_{30+30+10n}$, $C_{30+30+18n}$, and $C_{30+30+12n}$. Some studies pointed out that the D_{5h}-C_{90} and D_{5d}-C_{100} exhibit semiconducting electronic properties and metallic characteristics, respectively, manifesting a reductive energy band gap when the number

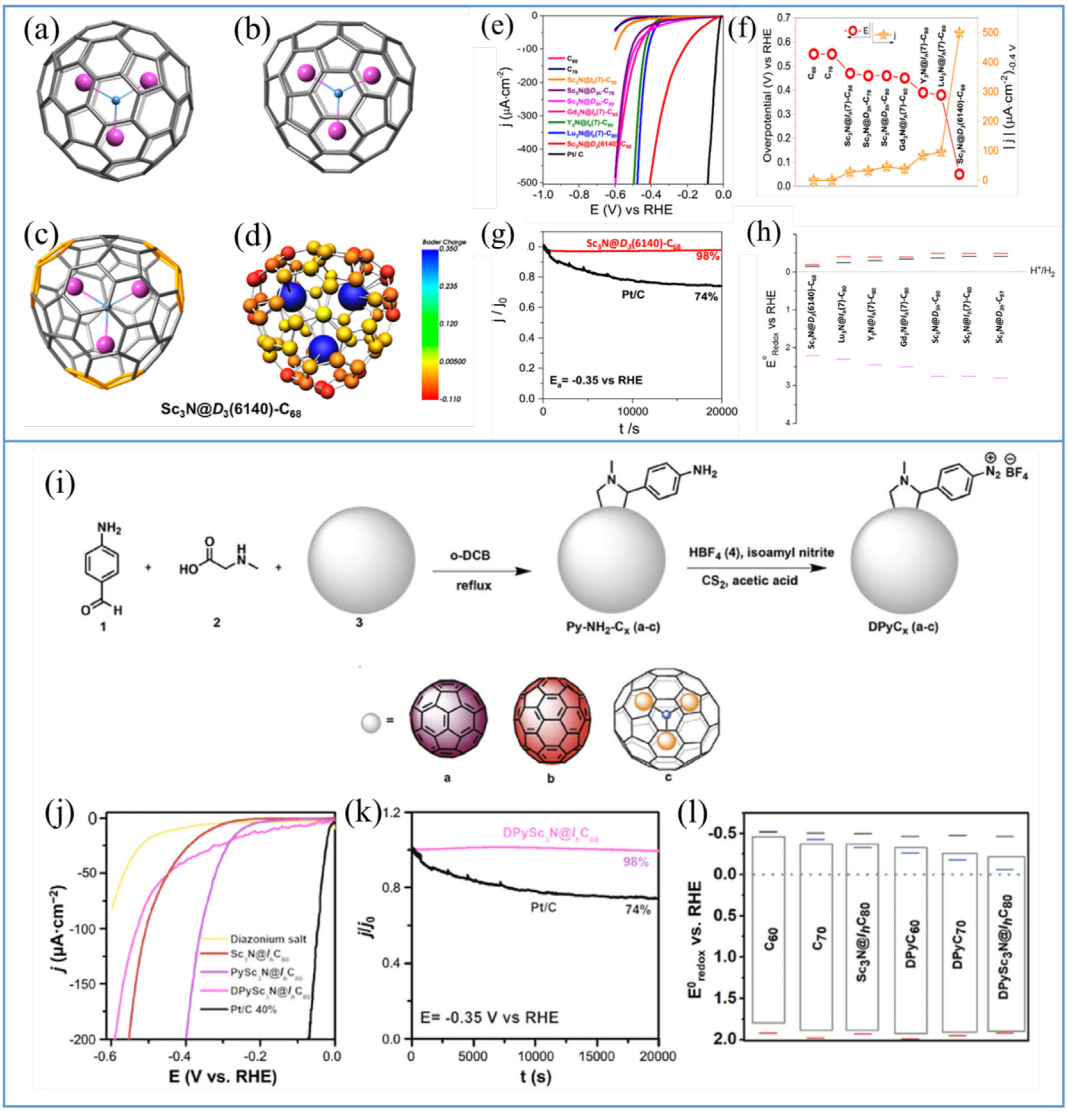

Fig. 11. Ball-and-stick representation for (a) $Sc_3N@I_h(7)$-C_{80}, (b) $Sc_3N@D_{3h}(5)$-C_{78}, and (c) $Sc_3N@D_3(6140)$-C_{68}. (d) Computed atomic charges for $Sc_3N@D_3(6140)$-C_{68}. (e) LSVs of HER and (f) onset overpotential and current density HER values for C_{60}, C_{70}, EMFs, and Pt/C in 0.5 M H_2SO_4 (g). (h) Mott-Schottky results of the EMFs. Reprinted with permission from Ref. [80]. Copyright (2021) American Chemical Society. (i) Illustration of the synthetic process of functionalized C_{60}, C_{70}, and $Sc_3N@IhC_{80}$. (j) LSV curves of HER. (k) *I–t* curves for DPy $Sc_3N@IhC_{80}$ and Pt/C. (l) Mott Schottky analyses of the functionalized EMFs. Reprinted with permission from Ref. [82]. Copyright (2022) Royal Society of Chemistry.

of carbon atoms increases [76,77]. While for the D_3 and $D_{3d/h}$ fullerenes (number of atoms: 60–150), the energy band gap reduces with the C atom number increases. However, the energy band gap D_{5h}-C_{100} is found larger than that of the D_{5h}-C_{90}, which is antipodal to the rules of D_3 and $D_{3d/h}$ fullerenes [78]. Thus, higher fullerenes that have larger carbon cage sizes not only visually display the size difference compared to the common C_{60} and C_{70} fullerene, but also exhibit complex electronic properties, which draw great attention to be used as potential electrocatalysts.

Luis Echegoyen and coworkers first explored the performance of three new synthetic fullertubes including C_{90}-D_{5h}, C_{96}-D_{3d}, and C_{100}-D_{5d} towards the ORR (Fig. 10c–e) [3]. One can clearly see in Fig. 10d that C_{96}-D_{3d} possesses the highest E_{on} (0.85 V vs. RHE) and $E_{1/2}$ (0.75 V vs. RHE) in 0.1 M KOH, and derives a high selectivity of four electron ORR. The theoretically calculated HOMO–LUMO gaps of these fullerenes in Fig. 10f show that the smallest band gap (1.15 eV) of C_{96}-D_{3d} is close to the ideal potential for water splitting and oxygen reduction, manifesting the promising ability of C_{96} for ORR. In another work, the HER activities of commercially available fullerenes (C_{60}, C_{70}, C_{76}, C_{84}, C_{100}) were used to recognize the electrocatalytic performance by simply loading the fullerenes ink on nickel foam [79]. The bandgap energies of C_{60}, C_{70}, C_{76}, $C_{84,}$ and C_{100} were calculated to be 2.77, 2.68, 1.98, 2.15, and 2.39 eV, respectively, which are in line with those reported in the literature (Fig. 10g and h). The lowest bandgap energy of C_{76} indicates its high conductivity, which ensures the most promising electrocatalyst of C_{76} among those samples. The Ni foam loaded with more C_{76} showed a sharply reduced overpotential (Fig. 10i). For example, the overpotential of nikel foam with 0.53 mg C_{76} loading is only 20 mV in 0.5 M H_2SO_4, which is much lower than the 0.12 mg C_{76} loading nickel foam (270 mV). Furthermore, all the C_{76} loading nickel foam samples exhibited a superior overpotential to the pristine C_{76} (420 mV). In the C_{76} and nickel foam composite, an interface dipole layer (IDL) was constructured via electrons transfer from nickel to C_{76} (Fig. 10j), which is proved by the ΔG_{*H} value for C_{76}/Ni foam (−0.09 eV, closet to zero) compared to the bare Ni foam (−0.43 eV), thus ensuring the enhanced HER activity of C_{76}/Ni foam (Fig. 10k). Moreover, it can also see that this exchange current of nickel foam loaded with 0.53 mg C_{76} incresaed by 5.99 A cm^{-2} compared to the bare nickel foam (Fig. 10l).

3.2.3. Endohedral fullerene and its derivates

DFT calculations have confirmed that encapsulated metals or metal compounds can break the initial electron distribution of the fullerene cage and further activate the fullerene molecules [10,38–41]. However, the extremely low yield of EMFs greatly impedes the wide application of electrocatalysts, and few works were reported in past decades. Recently, the amazing electronic distribution of EMFs draws tremendous attention from researchers. Up to now, some researchers start to explore the electrocatalytic performance of EMFs.

Echegoyen and co-workers first performed the DFT calculation of seven $M_3N@C_{2n}$ fullerenes as molecules for HER electrocatalyst [80]. Here, M represents Sc, Y, Gd, and Lu, and 2*n* represents 68, 78, and 80. The structural models of the three EMFs are shown in Fig. 11a–d. The electronic structures of $M_3N@C_{2n}$ can be understood with an ionic model of $(M_3N)^{6+}(C_{2n})^{6-}$, implying there is a six-electron transfer process from the internal cluster to the external fullerene cage [81]. Importantly, the peculiar structural features of $Sc_3N@D_3$ (6140)-C_{68} clearly show that the internal Sc atoms in the Sc_3N unit greatly affect the charge distribution of pentalene units in the external fullerene cage (Fig. 11c and d), resulting in pentalene units are negatively charged. Owing to the prominent electron transfer between the Sc_3N unit and the fullerene cage, the crucial process of hydrogen adsorption onto the fullerene cage is greatly improved. $Sc_3N@D_3$ (6140)-C_{68} exhibits the superior HER overpotential to the others, and performs reliable stability (Fig. 11e and f). Furthermore, the calculated Fermi level for $Sc_3N@D_3$ (6140)-C_{68} based on Mott Schottky (M−S) analysis is proximate to 0 eV (the ideal potential for hydrogen evolution), which further confirms the interactions between Sc ions and negatively charged pentalene can effectively enhance HER activity.

The selectivity addition reactions can introduce plentiful mono- and multiple functional groups to the surface of EMFs, which can not only regulate the chemical environment but also modify the localized charge distribution of EMFs. Such a functionalized strategy is a powerful way to promote electrocatalytic activity by improving the electronic configuration of pristine fullerene. Echegoyen and colleagues found that using diazonium salts to functionalize EMFs can introduce extremely high active sites into EMFs via changing the surface charge polarization states [82]. The functionalized $DPySc_3N@IhC_{80}$ exhibited the lowest onset potential of −0.25 V vs. RHE and excellent stability compared to other samples. Furthermore, the M−S analysis indicates $DPySc_3N@IhC_{80}$ has the lowest band gap and the Fermi level, which implies the diazonium group regulates the local charge distribution and the C atoms adjacent to the functional group are more negatively charged. Attributed to the changes after the introduction of the diazonium group, the HER activity of functional EMFs was promoted.

4. Conclusions and outlook

Great attention has been paid to fullerenes because of the special well-defined molecular and sp^2-hybridized carbon atoms. The regular fullerene C_{60} with ideal electron acceptors and semiconductor characteristics is most studied because of the sunken LUMO and large band energy gap. Many theoretical DFT works were performed to forecast the electrocatalytic activity of fullerenes and their derivates towards ORR, OER, and HER. It has been pointed out that both heteroatom doping and metal encapsulation are useful strategies to optimize the electrolytic activity by regulating the charge distribution or introducing active sites. On the other, for the case of practical applications of fullerenes and their derivates, researchers designed catalysts based on their intrinsic characteristics. The high electron affinity endows fullerenes with the potential of easily regulated electronic structure when they are composited with other materials, which further enlarges the application of electrocatalysts. The fullerene itself can also act as the electrocatalyst, the electrocatalytic activity of which can be further improved by the hybridization process due to the charge self-distribution after doping or functionalization. Such processes can not not only activate the inert fullerene cages by localized electron adjustment but also give rise to abundant fullerene derivatives. In addition, the π–π interaction between the fullerene molecules results in the formation of crystalline fullerene mico-/nano-structures in given solutions via a self-assembly process. In addition to the wide application of fullerenes in the field of ORR, OER, and HER, fullerenes also exhibit great potential for other energy field applications. For example, high temperature annealing Fc-C_{60} crystals can prepare a Fe and N co-doped carbons with excellent capacity in 6 M KOH [71], functional nitrofullerene can be used as additive into the electrolyte to stabilize the anode Lithuim (or sodium) and further to smooth the surface of the anode in Li (or Na)-ions batteries [83,84], fullerene-modified MOF-545-Co exhibits boosting CO_2 electroreduction performance [85], novel metal (Pt, Ru or Pd) decorated C_{60} displays outstanding methanol and ethanol oxidation fuel cells [86,87], and even the high value-added ethylene glycol can be electro-synthesized with C_{60}-buffered Cu/SiO_2 as catalyst [48]. Those applications of fullerenes greatly extend the scope of their use.

Although much progresses have been achieved in past decades, the wide application for ORR, OER, and HER of fullerenes is also faced with great challenges waiting to be settled down, and further exploration should be carried out. The limitations of current studies are listed below.

(1) Up to now, only the C_{60} and C_{70} can be scaled produced by an arc-discharge process, and the price of which is still relatively higher than the commercial graphene and other carbons, for example, CNTs, and hard carbon. The higher fullerene with superior catalytic activity including C_{76}, EMFs, and fullertubes is much more difficult to synthesize due to the limited synthetic process. Especially, although many metal-doped fullerenes are highly active electrocatalysts, they are never experimentally reported due to the

absence of actual materials. Those problems greatly impede the wide application of fullerenes and their derivates. If it can be properly solved, a great achievement will be made for the wide application.

(2) The fullerenes are commonly unsoluble in aqueous solutions where the ORR, OER, and HER take place, which results in extremely poor conductivity and sluggish reaction kinetics. Furthermore, fullerenes only dissolve in one of the few non-polar organic solvents, such as toluene. Thus, new methods to improve hydrophilia without pollution are highly desirable.

(3) Although fullerene composites, fullerene crystals, and higher fullerenes are confirmed with amazing electrocatalytic activity, the reaction active sites and intermediate are still unclear, which greatly restricts the depth of comprehension of the catalytic mechanism. More accurate and advanced techniques should be rationally developed to detect the reaction process and confirm the active sites, which can provide insight into the evolution of the interface, chemical, and electronic states as a function of the applied potential of these heterostructures.

Therefore, the principles for designing novel functional nanomaterials using fullerenes should take their advantages and limitations into account. First, great attention should be paid to the natural properties of fullerene molecules, such as their size, shape, and electronic characteristics, due to their diverse characteristics. Fullerenes with more carbon atoms have larger sizes and more complex electronic structures. Second, intrinsic fullerene molecules only possess C–C bonds and lack sufficient active groups, resulting in hydrophobic characteristics that impede their electrocatalytic activity. Chemical modifications on the surface of fullerene cages can impart specific functionalities, such as better solubility in different solvents (for example, water) or binding to specific targets. Third, micro-architectures, such as the atomic arrangement of fullerene molecules or multiple fullerene derivatives, should be highly considered because different micro-architectures can result in different specific surface areas and lattice structures. By fully understanding the properties of fullerenes and having in-depth insights into their catalytic mechanisms, fullerenes could be effective materials to overcome challenges in the field of electrocatalysts.

Author contributions

Y.Y. conceived the concept and led the project. A.Y. is responsible for the writing and modification of the manuscript. N.J. and W.Z. help with the modification of this manuscript. All authors approved the manuscript.

Declaration of competing interest

The authors declare no conflict of interest.

Acknowledgments

This work was supported by National Science Foundation (CMMI-1851674, CBET-1949840), and ACS PRF (65481-ND10). A.Y. acknowledges financial support from the Preeminent Postdoctoral Program (P3) at UCF.

References

[1] R. Gao, Q. Dai, F. Du, D. Yan, L. Dai, C_{60}-Adsorbed single-walled carbon nanotubes as metal-free, pH-universal, and multifunctional catalysts for oxygen reduction, oxygen evolution, and hydrogen evolution, J. Am. Chem. Soc. 141 (2019) 11658–11666.

[2] M.A. Ahsan, T. He, K. Eid, A.M. Abdullah, M.L. Curry, A. Du, A.R. Puente Santiago, L. Echegoyen, J.C. Noveron, Tuning the intermolecular electron transfer of low-dimensional and metal-free BCN/C_{60} electrocatalysts via interfacial defects for efficient hydrogen and oxygen electrochemistry, J. Am. Chem. Soc. 143 (2021) 1203–1215.

[3] M.F. Sanad, H.M. Franklin, B.A. Ali, A.R. Puente Santiago, A.N. Nair, V.S.N. Chava, O. Fernandez-Delgado, N.K. Allam, S. Stevenson, S.T. Sreenivasan, L. Echegoyen, Cylindrical C_{96} fullertubes: a highly active metal-free O_2-reduction electrocatalyst, Angew. Chem. Int. Ed. 61 (2022), e202116727.

[4] A. Yu, Z. Peng, Y. Li, L. Zhu, P. Peng, F.-F. Li, Fullerene-Derived carbon nanotubes and their electrocatalytic properties in oxygen reduction and Zn–air batteries, ACS Appl. Mater. Interfaces 14 (2022) 42337–42346.

[5] A.R. Puente Santiago, O. Fernandez-Delgado, A. Gomez, M.A. Ahsan, L. Echegoyen, Fullerenes as key components for low-dimensional (Photo)electrocatalytic nanohybrid materials, Angew. Chem. Int. Ed. 60 (2021) 122–141.

[6] Z. Peng, Q. Jiang, P. Peng, F.-F. Li, NH_3-activated fullerene derivative hierarchical microstructures to porous Fe_3O_4/N-C for oxygen reduction reaction and Zn-air battery, Engineered Sci 14 (2021) 27–38.

[7] K. Guo, N. Li, L. Bao, X. Lu, Fullerenes and Derivatives as Electrocatalysts: Promises and Challenges, Green Energy Environ, 2022, https://doi.org/10.1016/j.gee.2022.11.002.

[8] F. Gao, G.-L. Zhao, S. Yang, J.J. Spivey, Nitrogen-doped fullerene as a potential catalyst for hydrogen fuel cells, J. Am. Chem. Soc. 135 (2013) 3315–3318.

[9] X. Chen, H. Zhang, X. Li, Mechanisms of fullerene and single-walled carbon nanotube composite as the metal-free multifunctional electrocatalyst for the oxygen reduction, oxygen evolution, and hydrogen evolution, Mol. Catal. 502 (2021), 111383.

[10] X. Chen, S. Huang, H. Zhang, Bimetallic alloys encapsulated in fullerenes as efficient oxygen reduction or oxygen evolution reaction catalysts: a density functional theory study, J. Alloys Compd. 894 (2022), 162508.

[11] S. Salimi, N. Akbari, Z. Zand, M. Hołyńska, P. Aleshkevych, S.I. Allakhverdiev, M.M. Najafpour, Nanostructured manganese oxide on fullerene soot for water oxidation under neutral conditions, Int. J. Hydrogen Energy 48 (2023) 14199–14209.

[12] Y.-H. Choi, J. Lee, A. Parija, J. Cho, S.V. Verkhoturov, M. Al-Hashimi, L. Fang, S. Banerjee, An in situ sulfidation approach for the integration of MoS_2 nanosheets on carbon fiber paper and the modulation of its electrocatalytic activity by interfacing with nC60, ACS Catal. 6 (2016) 6246–6254.

[13] G. Saianand, A.-I. Gopalan, J.-C. Lee, C. Sathish, K. Gopalakrishnan, G.E. Unni, D. Shanbhag, V.D.B.C. Dasireddy, J. Yi, S. Xi, A.a.H. Al-Muhtaseb, A. Vinu, Mixed copper/copper-oxide anchored mesoporous fullerene nanohybrids as superior electrocatalysts toward oxygen reduction reaction, Small 16 (2020), 1903937.

[14] T. Luo, J. Huang, Y. Hu, C. Yuan, J. Chen, L. Cao, K. Kajiyoshi, Y. Liu, Y. Zhao, Z. Li, Y. Feng, Fullerene lattice-confined Ru nanoparticles and single atoms synergistically boost electrocatalytic hydrogen evolution reaction, Adv. Funct. Mater. 33 (2023), 2213058.

[15] T. Xu, W. Shen, W. Huang, X. Lu, Fullerene micro/nanostructures: controlled synthesis and energy applications, Mater, Today Nano 11 (2020), 100081.

[16] A. Zieleniewska, F. Lodermeyer, A. Roth, D.M. Guldi, Fullerenes – how 25 years of charge transfer chemistry have shaped our understanding of (interfacial) interactions, Chem. Soc. Rev. 47 (2018) 702–714.

[17] M.D. Diener, J.M. Alford, Isolation and properties of small-bandgap fullerenes, Nature 393 (1998) 668–671.

[18] Y. Yang, F. Arias, L. Echegoyen, L.P.F. Chibante, S. Flanagan, A. Robertson, L.J. Wilson, Reversible fullerene electrochemistry: correlation with the HOMO-LUMO energy difference for C_{60}, C_{70}, C_{76}, C_{78}, and C_{84}, J. Am. Chem. Soc. 117 (1995) 7801–7804.

[19] W.H. Green, S.M. Gorun, G. Fitzgerald, P.W. Fowler, A. Ceulemans, B.C. Titeca, Electronic structures and geometries of C_{60} anions via density functional calculations, J. Phys. Chem. 100 (1996) 14892–14898.

[20] M. Yoshida, J.-i. Aihara, Validity of the weighted HOMO–LUMO energy separation as an index of kinetic stability for fullerenes with up to 120 carbon atoms, Phys. Chem. Chem. Phys. 1 (1999) 227–230.

[21] Z. Li, B. Li, M. Yu, C. Yu, P. Shen, Amorphous metallic ultrathin nanostructures: a latent ultra-high-density atomic-level catalyst for electrochemical energy conversion, Int. J. Hydrogen Energy 47 (2022) 26956–26977.

[22] Y. He, L. Liu, C. Zhu, S. Guo, P. Golani, B. Koo, P. Tang, Z. Zhao, M. Xu, C. Zhu, P. Yu, X. Zhou, C. Gao, X. Wang, Z. Shi, L. Zheng, J. Yang, B. Shin, J. Arbiol, H. Duan, Y. Du, M. Heggen, R.E. Dunin-Borkowski, W. Guo, Q.J. Wang, Z. Zhang, Z. Liu, Amorphizing noble metal chalcogenide catalysts at the single-layer limit towards hydrogen production, Nat. Catal. 5 (2022) 212–221.

[23] H. Cheng, N. Yang, G. Liu, Y. Ge, J. Huang, Q. Yun, Y. Du, C.-J. Sun, B. Chen, J. Liu, H. Zhang, Ligand-exchange-induced amorphization of Pd nanomaterials for highly efficient electrocatalytic hydrogen evolution reaction, Adv. Mater. 32 (2020), 1902964.

[24] W. Zhang, J. Chang, G. Wang, Z. Li, M. Wang, Y. Zhu, B. Li, H. Zhou, G. Wang, M. Gu, Z. Feng, Y. Yang, Surface oxygenation induced strong interaction between Pd catalyst and functional support for zinc–air batteries, Energy Environ. Sci. 15 (2022) 1573–1584.

[25] W. Zhang, J. Chang, Y. Yang, Strong precious metal–metal oxide interaction for oxygen reduction reaction: a strategy for efficient catalyst design, SusMat 3 (2023) 2–20.

[26] J.K. Nørskov, J. Rossmeisl, A. Logadottir, L. Lindqvist, J.R. Kitchin, T. Bligaard, H. Jónsson, Origin of the overpotential for oxygen reduction at a fuel-cell cathode, J. Phys. Chem. B 108 (2004) 17886–17892.

[27] Y. Lin, D. Su, Fabrication of nitrogen-modified annealed nanodiamond with improved catalytic activity, ACS Nano 8 (2014) 7823–7833.

[28] S. Gao, X. Wei, H. Fan, L. Li, K. Geng, J. Wang, Nitrogen-doped carbon shell structure derived from natural leaves as a potential catalyst for oxygen reduction reaction, Nano Energy 13 (2015) 518–526.

[29] X. Chen, J. Chang, Q. Ke, Probing the activity of pure and N-doped fullerenes towards oxygen reduction reaction by density functional theory, Carbon 126 (2018) 53–57.
[30] Y. Wang, M. Jiao, W. Song, Z. Wu, Doped fullerene as a metal-free electrocatalyst for oxygen reduction reaction: a first-principles study, Carbon 114 (2017) 393–401.
[31] Q.-Z. Li, J.-J. Zheng, J.-S. Dang, X. Zhao, Boosting activation of oxygen molecules on C_{60} fullerene by boron doping, ChemPhysChem 16 (2015) 390–395.
[32] S. Yang, Y. Cheng, H. Liu, X. Huang, Heteroatom-doped fullerene C_{70} as non-metal electrocatalysts for oxygen reduction and oxygen evolution from computational study, Diam. Relat. Mater. 124 (2022), 108954.
[33] J. Rossmeisl, A. Logadottir, J.K. Nørskov, Electrolysis of water on (oxidized) metal surfaces, Chem. Phys. 319 (2005) 178–184.
[34] X. Chen, F. Ge, J. Chang, N. Lai, Exploring the catalytic activity of metal-fullerene $C_{58}M$ (M = Mn, Fe, Co, Ni, and Cu) toward oxygen reduction and CO oxidation by density functional theory, Int. J. Energy Res. 43 (2019) 7375–7383.
[35] A. Yu, W. Long, L. Zhu, Y. Zhao, P. Peng, F.-F. Li, Transformation of postsynthesized F-MOF to Fe/N/F-tridoped carbon nanotubes as oxygen reduction catalysts for high power density Zn-air batteries, Chin. Chem. Lett. 34 (2023), 107860.
[36] A. Yu, Z. Peng, Y. Li, L. Zhu, P. Peng, F.-F. Li, Fullerene-Derived carbon nanotubes and their electrocatalytic properties in oxygen reduction and Zn–air batteries, ACS Appl. Mater. Interfaces 14 (2022) 42337–42346.
[37] J. Rong, E. Gao, N. Liu, W. Chen, X. Rong, Y. Zhang, X. Zheng, H. Ao, S. Xue, B. Huang, Z. Li, F. Qiu, Y. Qian, Porphyrinic MOF-derived rich N-doped porous carbon with highly active CoN_4C single-atom sites for enhanced oxygen reduction reaction and Zn-air batteries performance, Energy Storage Mater. 56 (2023) 165–173.
[38] S. Yang, C. Zhao, R. Qu, Y. Cheng, H. Liu, X. Huang, Probing the activity of transition metal M and heteroatom N_4 co-doped in vacancy fullerene ($M–N_4–C_{64}$, M = Fe, Co, and Ni) towards the oxygen reduction reaction by density functional theory, RSC Adv. 11 (2021) 3174–3182.
[39] X. Chen, H. Zhang, N. Lai, Endohedral metallofullerenes $Mn@C_{60}$ (M = Mn, Co, Ni, Cu; n = 2–5) as electrocatalysts for oxygen reduction reaction: a first-principles study, J. Mater. Sci. 55 (2020) 11382–11390.
[40] X. Chen, F. Ge, N. Lai, Probing the catalytic activity and poisoning-tolerance ability of endohedral metallofullerene $fen@C_{60}$ (n = 1−7) catalysts in the oxygen reduction reaction, J. Electrochem. Soc. 167 (2020), 024515.
[41] T. He, G. Gao, L. Kou, G. Will, A. Du, Endohedral metallofullerenes ($M@C_{60}$) as efficient catalysts for highly active hydrogen evolution reaction, J. Catal. 354 (2017) 231–235.
[42] E.C. Agwamba, H. Louis, B.B. Isang, G.J. Ogunwale, O.J. Ikenyirimba, A.S. Adeyinka, Pristine fullerene (C_{24}) metals (Mo, Fe, Au) engineered nanostructured materials as an efficient electro-catalyst for hydrogen evolution reaction (HER): a density functional theory (DFT) study, Mater. Chem. Phys. 297 (2023), 127374.
[43] Y. Feng, X. Wang, J. Huang, P. Dong, J. Ji, J. Li, L. Cao, L. Feng, P. Jin, C. Wang, Decorating CoNi layered double hydroxides nanosheet arrays with fullerene quantum dot anchored on Ni foam for efficient electrocatalytic water splitting and urea electrolysis, Chem. Eng. J. 390 (2020), 124525.
[44] A. Hasanzadeh, A. Khataee, M. Zarei, Y. Zhang, Two-electron oxygen reduction on fullerene C_{60}-carbon nanotubes covalent hybrid as a metal-free electrocatalyst, Sci. Rep. 9 (2019), 13780.
[45] T. Munawar, A. Bashir, M.S. Nadeem, F. Mukhtar, S. Manzoor, M.N. Ashiq, S.A. Khan, M. Koc, F. Iqbal, Electrochemical performance evaluation of bimetallic sulfide nanocomposite with fullerene (CeNdS/C60) for efficient oxygen evolution reaction (OER), Energy Fuels 37 (2023) 1370–1386.
[46] A. Bashir, T. Munawar, F. Mukhtar, M.S. Nadeem, S. Manzoor, M.N. Ashiq, S.A. Khan, M. Koc, F. Iqbal, Dual-functional fullerene supported NiO-based nanocomposite: efficient electrocatalyst for OER and photocatalyst for MB dye degradation, Mater. Chem. Phys. 293 (2023), 126886.
[47] A.R. Puente Santiago, T. He, O. Eraso, M.A. Ahsan, A.N. Nair, V.S.N. Chava, T. Zheng, S. Pilla, O. Fernandez-Delgado, A. Du, S.T. Sreenivasan, L. Echegoyen, Tailoring the interfacial interactions of van der Waals 1T-MoS_2/C_{60} heterostructures for high-performance hydrogen evolution reaction electrocatalysis, J. Am. Chem. Soc. 142 (2020) 17923–17927.
[48] J. Zheng, L. Huang, C.-H. Cui, Z.-C. Chen, X.-F. Liu, X. Duan, X.-Y. Cao, T.-Z. Yang, H. Zhu, K. Shi, P. Du, S.-W. Ying, C.-F. Zhu, Y.-G. Yao, G.-C. Guo, Y. Yuan, S.-Y. Xie, L.-S. Zheng, Ambient-pressure synthesis of ethylene glycol catalyzed by C_{60}-buffered Cu/SiO_2, Science 376 (2022) 288–292.
[49] A.G. Nasibulin, P.V. Pikhitsa, H. Jiang, D.P. Brown, A.V. Krasheninnikov, A.S. Anisimov, P. Queipo, A. Moisala, D. Gonzalez, G. Lientschnig, A. Hassanien, S.D. Shandakov, G. Lolli, D.E. Resasco, M. Choi, D. Tománek, E.I. Kauppinen, A novel hybrid carbon material, Nat. Nanotechnol. 2 (2007) 156–161.
[50] D.D. Chronopoulos, C. Stangel, M. Scheibe, K. Čépe, N. Tagmatarchis, M. Otyepka, Electrocatalytic activity for proton reduction by a covalent non-metal graphene–fullerene hybrid, Chem. Commun. 58 (2022) 8396–8399.
[51] T.F. Jaramillo, K.P. Jørgensen, J. Bonde, J.H. Nielsen, S. Horch, I. Chorkendorff, Identification of active edge sites for electrochemical H_2 evolution from MoS_2 nanocatalysts, Science 317 (2007) 100–102.
[52] B. Hinnemann, P.G. Moses, J. Bonde, K.P. Jørgensen, J.H. Nielsen, S. Horch, I. Chorkendorff, J.K. Nørskov, Biomimetic hydrogen evolution: MoS_2 nanoparticles as catalyst for hydrogen evolution, J. Am. Chem. Soc. 127 (2005) 5308–5309.
[53] R. Chen, C. Lin, H. Yu, Y. Tang, C. Song, L. Yuwen, H. Li, X. Xie, L. Wang, W. Huang, Templating C_{60} on MoS_2 nanosheets for 2D hybrid van der Waals p–n nanoheterojunctions, Chem. Mater. 28 (2016) 4300–4306.
[54] H. Kuzmany, M. Matus, B. Burger, J. Winter, Raman Scattering in C_{60} fullerenes and fullerides, Adv. Mater. 6 (1994) 731–745.
[55] K. Ding, J. Hu, W. Jin, L. Zhao, Y. Liu, Z. Wu, B. Weng, H. Hou, X. Ji, Dianion induced electron delocalization of trifunctional electrocatalysts for rechargeable Zn–air batteries and self-powered water splitting, Adv. Funct. Mater. 32 (2022), 2201944.
[56] Y. Zheng, Y. Jiao, Y. Zhu, L.H. Li, Y. Han, Y. Chen, M. Jaroniec, S.-Z. Qiao, High electrocatalytic hydrogen evolution activity of an anomalous ruthenium catalyst, J. Am. Chem. Soc. 138 (2016) 16174–16181.
[57] M. Sathish, K.i. Miyazawa, J.P. Hill, K. Ariga, Solvent engineering for shape-shifter pure fullerene (C_{60}), J. Am. Chem. Soc. 131 (2009) 6372–6373.
[58] L.K. Shrestha, Y. Yamauchi, J.P. Hill, K.i. Miyazawa, K. Ariga, Fullerene crystals with bimodal pore architectures consisting of macropores and mesopores, J. Am. Chem. Soc. 135 (2013) 586–589.
[59] P. Bairi, K. Minami, W. Nakanishi, J.P. Hill, K. Ariga, L.K. Shrestha, Hierarchically structured fullerene C_{70} cube for sensing volatile aromatic solvent vapors, ACS Nano 10 (2016) 6631–6637.
[60] S. Zheng, N.T. Cuong, S. Okada, T. Xu, W. Shen, X. Lu, K. Tsukagoshi, Solvent-mediated shape engineering of fullerene (C_{60}) polyhedral microcrystals, Chem. Mater. 30 (2018) 7146–7153.
[61] P. Bairi, T. Tsuruoka, S. Acharya, Q. Ji, J.P. Hill, K. Ariga, Y. Yamauchi, L.K. Shrestha, Mesoporous fullerene C_{70} cubes with highly crystalline frameworks and unusually enhanced photoluminescence properties, Mater. Horiz. 5 (2018) 285–290.
[62] F. Han, R. Wang, Y. Feng, S. Wang, L. Liu, X. Li, Y. Han, H. Chen, On demand synthesis of hollow fullerene nanostructures, Nat. Commun. 10 (2019) 1548.
[63] O. Fernandez-Delgado, A.R. Puente-Santiago, M. Cano, J.J. Giner-Casares, A.J. Metta-Magaña, L. Echegoyen, Facile synthesis of C_{60}-nano materials and their application in high-performance water splitting electrocatalysis, Sustain. Energy Fuels 4 (2020) 2900–2906.
[64] M. Yao, B.M. Andersson, P. Stenmark, B. Sundqvist, B. Liu, T. Wågberg, Synthesis and growth mechanism of differently shaped C_{60} nano/microcrystals produced by evaporation of various aromatic C_{60} solutions, Carbon 47 (2009) 1181–1188.
[65] R. Colle, G. Grosso, A. Ronzani, M. Gazzano, V. Palermo, Anisotropic molecular packing of soluble C_{60} fullerenes in hexagonal nanocrystals obtained by solvent vapor annealing, Carbon 50 (2012) 1332–1337.
[66] C. Larsen, H.R. Barzegar, F. Nitze, T. Wågberg, L. Edman, On the fabrication of crystalline C_{60} nanorod transistors from solution, Nanotechnology 23 (2012), 344015.
[67] J.A. Rather, A.J. Al Harthi, E.A. Khudaish, A. Qurashi, A. Munam, P. Kannan, An electrochemical sensor based on fullerene nanorods for the detection of paraben, an endocrine disruptor, Anal. Methods 8 (2016) 5690–5700.
[68] L. Yang, J. Shui, L. Du, Y. Shao, J. Liu, L. Dai, Z. Hu, Carbon-based metal-free ORR electrocatalysts for fuel cells: past, present, and future, Adv. Mater. 31 (2019), 1804799.
[69] D. Liu, X. Li, S. Chen, H. Yan, C. Wang, C. Wu, Y.A. Haleem, S. Duan, J. Lu, B. Ge, P.M. Ajayan, Y. Luo, J. Jiang, L. Song, Atomically dispersed platinum supported on curved carbon supports for efficient electrocatalytic hydrogen evolution, Nat. Energy 4 (2019) 512–518.
[70] M.R. Benzigar, S. Joseph, A.V. Baskar, D.-H. Park, G. Chandra, S. Umapathy, S.N. Talapaneni, A. Vinu, Ordered mesoporous C_{70} with highly crystalline pore walls for energy applications, Adv. Funct. Mater. 28 (2018), 1803701.
[71] Z.Y. Peng, Y.J. Hu, J.J. Wang, S.J. Liu, C.X. Li, Q.L. Jiang, J. Lu, X.Q. Zeng, P. Peng, F.-F. Li, Fullerene-based in situ doping of N and Fe into a 3D cross-like hierarchical carbon composite for high-performance supercapacitors, Adv. Energy Mater. 9 (2019), 1802928.
[72] W. Zhao, P. Yuan, X. She, Y. Xia, S. Komarneni, K. Xi, Y. Che, X. Yao, D. Yang, Sustainable seaweed-based one-dimensional (1D) nanofibers as high-performance electrocatalysts for fuel cells, J. Mater. Chem. 3 (2015) 14188–14194.
[73] Z. He, P. Wei, N. Chen, J. Han, X. Lu, N,S-Co-Doped porous carbon nanofiber films derived from fullerenes (C60) as efficient electrocatalysts for oxygen reduction and a Zn–air battery, Chem. Eur J. 27 (2021) 1423–1429.
[74] Z. He, Z. Zhou, P. Wei, T. Xu, J. Han, K. Huang, K. Guo, W. Huang, T. Akasaka, X. Lu, Fullerene-Derived porous and defective N-doped carbon nanosheets as advanced trifunctional metal-free electrocatalysts, Chem. Asian J. 18 (2023), e202200994.
[75] R.M. Koenig, H.-R. Tian, T.L. Seeler, K.R. Tepper, H.M. Franklin, Z.-C. Chen, S.-Y. Xie, S. Stevenson Fullertubes, Cylindrical carbon with half-fullerene end-caps and tubular graphene belts, their chemical enrichment, crystallography of pristine C_{90}-d5h(1) and C_{100}-d5d(1) fullertubes, and isolation of C_{108}, C_{120}, C_{132}, and C_{156} cages of unknown structures, J. Am. Chem. Soc. 142 (2020) 15614–15623.
[76] S. Stevenson, X. Liu, D.M. Sublett Jr., R.M. Koenig, T.L. Seeler, K.R. Tepper, H.M. Franklin, X. Wang, R. Huang, X. Feng, K. Cover, D. Troya, N. Shanaiah, R.J. Bodnar, H.C. Dorn, Semiconducting and metallic [5,5] fullertube nanowires: characterization of pristine $d_{5h(1)}$-C_{90} and $_{d5d(1)}$-C_{100}, J. Am. Chem. Soc. 143 (2021) 4593–4599.
[77] X. Liu, E. Bourret, C.A. Noble, K. Cover, R.M. Koenig, R. Huang, H.M. Franklin, X. Feng, R.J. Bodnar, F. Zhang, C. Tao, D.M. Sublett Jr., H.C. Dorn, S. Stevenson, Gigantic C_{120} fullertubes: prediction and experimental evidence for isomerically purified metallic [5,5] $C_{120\text{-}d5d(1)}$ and nonmetallic [10,0] $C_{120\text{-}d5h(10766)}$, J. Am. Chem. Soc. 144 (2022) 16287–16291.
[78] C.M. Schüßlbauer, M. Krug, T. Ullrich, H.M. Franklin, S. Stevenson, T. Clark, D.M. Guldi, Exploring the threshold between fullerenes and nanotubes: characterizing isomerically pure, empty-caged, and tubular fullerenes $D_{5h\text{-}C90}$ and D_{5d}-C_{100}, J. Am. Chem. Soc. 144 (2022) 10825–10829.

[79] M.M. Hasan, G.E. Khedr, N.K. Allam, C_{76} nanospheres/Ni foam as high-performance heterostructured electrocatalysts for hydrogen evolution reaction: unveiling the interfacial interaction, ACS Appl. Nano Mater. 5 (2022) 15457–15464.
[80] A.R. Puente Santiago, M.F. Sanad, A. Moreno-Vicente, M.A. Ahsan, M.R. Cerón, Y.-R. Yao, S.T. Sreenivasan, A. Rodriguez-Fortea, J.M. Poblet, L. Echegoyen, A new class of molecular electrocatalysts for hydrogen evolution: catalytic activity of $M_3N@C_{2n}$ (2n = 68, 78, and 80) fullerenes, J. Am. Chem. Soc. 143 (2021) 6037–6042.
[81] M.N. Chaur, R. Valencia, A. Rodríguez-Fortea, J.M. Poblet, L. Echegoyen, Trimetallic nitride endohedral fullerenes: experimental and theoretical evidence for the $M_3N^{6+}@C_{2n}^{6-}$ model, Angew. Chem., Int. Ed. 48 (2009) 1425–1428.
[82] O. Fernandez-Delgado, A.R. Puente Santiago, J. Galindo Betancourth, M.F. Sanad, S.T. Sreenivasan, L. Echegoyen, Diazonium functionalized fullerenes: a new class of efficient molecular catalysts for the hydrogen evolution reaction, Nanoscale 14 (2022) 3858–3864.
[83] P. Li, Z. Jiang, X. Huang, X. Lu, J. Xie, S. Cheng, Nitrofullerene as an electrolyte-compatible additive for high-performance sodium metal batteries, Nano Energy 89 (2021), 106396.
[84] Z. Jiang, Z. Zeng, C. Yang, Z. Han, W. Hu, J. Lu, J. Xie, Nitrofullerene, a C_{60}-based bifunctional additive with smoothing and protecting effects for stable lithium metal anode, Nano Lett. 19 (2019) 8780–8786.
[85] X. Dong, Z. Xin, D. He, J.-L. Zhang, Y.-Q. Lan, Q.-F. Zhang, Y. Chen, Boosting CO_2 electroreduction performance over fullerene-modified MOF-545-Co promoted by π–π interaction, Chin. Chem. Lett. 34 (2023), 107459.
[86] G. Lee, J.H. Shim, H. Kang, K.M. Nam, H. Song, J.T. Park, Monodisperse, Pt and PtRu/C_{60} hybrid nanoparticles for fuel cell anode catalysts, Chem. Commun. (2009) 5036–5038.
[87] Q. Zhang, Z. Bai, M. Shi, L. Yang, J. Qiao, K. Jiang, High-efficiency palladium nanoparticles supported on hydroxypropyl-β-cyclodextrin modified fullerene [60] for ethanol oxidation, Electrochim. Acta 177 (2015) 113–117.